



## New minerals in type A inclusions from Allende and clues to processes in the early solar system: Paqueite, $\text{Ca}_3\text{TiSi}_2(\text{Al,Ti,Si})_3\text{O}_{14}$ , and burnettite, $\text{CaVAISiO}_6$

Chi MA <sup>\*</sup>1, John R. BECKETT<sup>1</sup>, François L. H. TISSOT <sup>2</sup>, and George R. ROSSMAN<sup>1</sup>

<sup>1</sup>Division of Geological and Planetary Sciences, California Institute of Technology, Pasadena, California 91125, USA

<sup>2</sup>The Isotoparium, Division of Geological and Planetary Sciences, California Institute of Technology, Pasadena, California 91125, USA

\*Corresponding author. E-mail: chima@caltech.edu

(Received 14 October 2021; revision accepted 12 April 2022)

**Abstract**—Paqueite ( $\text{Ca}_3\text{TiSi}_2[\text{Al,Ti,Si}]_3\text{O}_{14}$ ; IMA 2013-053) and burnettite ( $\text{CaVAISiO}_6$ ; IMA 2013-054) are new refractory minerals, occurring as euhedral to subhedral crystals within aluminous melilite in A-WP1, a type A Ca-Al-rich inclusion, and *CGft-12*, a compact type A (CTA) from the Allende CV3 carbonaceous chondrite. Type paqueite from A-WP1 has an empirical formula of  $(\text{Ca}_{2.91}\text{Na}_{0.11})\text{Ti}^{4+}\text{Si}_2(\text{Al}_{1.64}\text{Ti}^{4+}_{0.90}\text{Si}_{0.24}\text{V}^{3+}_{0.12}\text{Sc}_{0.07}\text{Mg}_{0.03})\text{O}_{14}$ , with a trigonal structure in space group *P321* and cell parameters  $a = 7.943 \text{ \AA}$ ,  $c = 4.930 \text{ \AA}$ ,  $V = 269.37 \text{ \AA}^3$ , and  $Z = 1$ . Paqueite's general formula is  $\text{Ca}_3\text{TiSi}_2(\text{Al,Ti,Si})_3\text{O}_{14}$  and the endmember formula is  $\text{Ca}_3\text{TiSi}_2(\text{Al}_2\text{Ti})\text{O}_{14}$ . Type burnettite from *CGft-12* has an empirical formula of  $\text{Ca}_{1.01}(\text{V}^{3+}_{0.56}\text{Al}_{0.25}\text{Mg}_{0.18})(\text{Si}_{1.19}\text{Al}_{0.81})\text{O}_6$ . It assumes a diopside-type *C2/c* structure with  $a = 9.80 \text{ \AA}$ ,  $b = 8.85 \text{ \AA}$ ,  $c = 5.36 \text{ \AA}$ ,  $\beta = 105.6^\circ$ ,  $V = 447.7 \text{ \AA}^3$ , and  $Z = 4$ . Burnettite's general formula is  $\text{Ca}(\text{V,Al,Mg})\text{AlSiO}_6$  and the endmember formula is  $\text{CaVAISiO}_6$ . Paqueite and burnettite likely originated as condensates, but the observed grains may have crystallized from local V-rich melts produced during a later thermal event. For *CGft-12*, the compositions of paqueite, clinopyroxene, and perovskite suggest that type A drew from two distinct populations of grains. Hibonite grains drew from multiple populations, but these were well mixed and not equilibrated prior to incorporation into type A host melilite.

### INTRODUCTION

Ca-Al-rich inclusions (CAIs) in meteorites are the products of processes that occurred during the early evolution of the solar system. Although bulk compositions of these objects provide some clues to process (e.g., Beckett & Grossman, 1988; Grossman et al., 2000), it is in the constituent minerals that most of the information lies. New minerals present opportunities to examine responses to aspects of environments that may have been less well recorded, or even gone unrecorded, by the other phases present in an inclusion (e.g., Ma et al., 2014b).

Allende fluffy type A (FTA) inclusions are CAIs uniquely posed to explore processes in the early solar system, both in the nebular environments where they presumably formed and in planetary settings, where they were commonly metasomatized (Krot et al., 2021;

MacPherson & Grossman, 1984). However, their potentially complex histories also pose problems in interpretation. It is, for example, known that oxygen isotopic distributions in melilite from FTAs tend to be sharply divided between relatively  $^{16}\text{O}$ -rich and  $^{16}\text{O}$ -poor regions (Katayama et al., 2012; Kawasaki et al., 2012), as is also observed for Al-Mg isotopic compositions (Kawasaki et al., 2017). These observations have been interpreted both in terms of changing oxygen reservoirs during condensation of melilite within the solar nebula and metasomatic alteration on a parent body (e.g., Kawasaki et al., 2017; Krot et al., 2008). FTA inclusions are especially important CAIs because they are composed primarily of coarse-grained melilite crystals that may be direct vapor to solid condensates (e.g., Kawasaki et al., 2017; MacPherson & Grossman, 1984). If so, the large grain sizes offer analytical opportunities that are absent in fine-grained, nonigneous inclusions. Moreover,

inclusions in a condensate melilite provide information on condensation, metamorphic, and/or partial melting processes that predate the host melilite.

Like FTAs, compact type A (CTA) inclusions consist mostly of coarse-grained melilite, but these objects were heated enough to cause substantial to complete melting, and volatilization with large losses of Mg and Si, as evidenced by enrichments in the heavy isotopes of these elements (e.g., Clayton et al., 1988; Grossman et al., 2008; Mendybaev et al., 2017). CTAs were subsequently heated again (e.g., Davis et al., 2010; Jacobsen et al., 2008), sometimes resulting in recrystallization of melilite and sometimes in partial to complete melting and partial exchange of oxygen isotopes (e.g., Aléon et al., 2018; Grossman et al., 2000; Simon et al., 1999; Suzumura et al., 2021). This later event(s) would have overprinted features produced by or preceding major Mg-Si volatilization. Thus, some CTAs display axiolic growth textures of melilite, indicative of crystallization from a melt, whereas, in others, melilite crystals have straight grain boundaries and 120° triple junctions, indicative of metamorphic recrystallization. Both FTAs and CTAs generally contain inclusions of spinel, perovskite, hibonite, metal alloys, and davisite/grossmanite. CTAs may contain grains predating the melting event(s), so that the inclusions potentially provide evidence for conditions before, during, and after the most recent major thermal event.

Phase compositions and mineral assemblages in CTAs and FTAs are similar, but there are some notable exceptions. For example, rhönite is observed in some CTAs (e.g., Floss et al., 2004; Fuchs, 1971; Simon et al., 1999; Teshima & Wasserburg, 1985), but has not been reported in FTAs, although FTAs occasionally contain the structurally related phase, addibischhoffite (Ma et al., 2017). Melilite compositions overlap, but the most magnesian melilites are invariably found in CTAs and the most aluminous in FTAs (e.g., MacPherson & Grossman, 1984).

Vanadium is an underappreciated indicator element in nebular environments. It is moderately refractory and present at wt% levels in both refractory and ultrarefractory phases such as clinopyroxene, hibonite, perovskite, spinel, and warkite in CAIs (e.g., Allen et al., 1978; Armstrong et al., 1985; El Goresy et al., 2002; Ma et al., 2020; Simon et al., 1996). Yet, it is often not even analyzed. This lack of respect may stem from the flexibility of V in responding to a wide variety of environments. Indeed, vanadium can substitute into high-temperature, primary phases, but it is also found in high concentrations in secondary phases like magnetite (e.g., Armstrong et al., 1985; Ma et al., 2014a, 2014b). In this work and the companion paper (Ma et al., 2021), we take advantage of the wide

distribution of V among phases in Allende type A inclusions to establish some basic constraints on the behavior of V in the nebula and, after accretion, on the Allende parent body, and use V, along with other elements, to infer sequences of events and sources of material reflected in the observed inclusions.

During a nanomineralogy investigation of type A inclusions in the Allende CV3 meteorite, we discovered three new minerals, paqueite ( $\text{Ca}_3\text{TiSi}_2[\text{Al,Ti,Si}]_3\text{O}_{14}$ ), burnettite ( $\text{CaV}^{3+}\text{AlSiO}_6$ ), and beckettite ( $\text{Ca}_2\text{V}^{3+}_6\text{Al}_6\text{O}_{20}$ ), and the terrestrially known but new-to-meteorite mineral baghdadite ( $\text{Ca}_3[\text{Zr,Ti}]\text{Si}_2\text{O}_9$ ). These phases all occur in a V-rich, type A inclusion A-WP1 from USNM 7617 and two (paqueite and burnettite) occur in *CGft-12*, an Allende CTA (Fig. 1). A-WP1 was previously studied by Paque (1985, 1989) and Paque et al. (1986, 1994, 2008). These authors referred to this heavily altered inclusion as an FTA. However, in view of the unusually large melilite crystals (200–400  $\mu\text{m}$ ) and unusual included phases, we use a less specific term, type A, for this inclusion.

In this work, we emphasize the chemistry, structure, and petrologic context for two of the new minerals:

1. Paqueite is a new Ca-, Ti-rich silicate mineral. Chemically similar phases have been studied in a variety of CAIs from carbonaceous chondrites (e.g., Caillet Komorowski et al., 2007; El Goresy et al., 1984; Krot et al., 2007; Paque et al., 1994) and in run products from synthetic systems (Barber & Agrell, 1994; Barber et al., 1994; Beckett & Stolper, 1994; Scheuermann et al., 2000).
2. Burnettite is a V-rich clinopyroxene and a new member of the diopside group. It has been synthesized (Taran & Ohashi, 2012) but not previously described in a natural setting.

In the present study, we describe paqueite and burnettite in the type A inclusion A-WP1 and CTA *CGft-12* and consider their origin(s) and implications for the evolution of CAIs and, especially of type As, in the early solar system. Preliminary results of this work are given by Ma and Beckett (2016). Beckettite, a third new refractory mineral discovered in A-WP1, is the subject of a companion paper (Ma et al., 2021). Baghdadite, which occurs as a single grain in A-WP1 (Ma, 2018), will be described in a separate publication.

## MINERAL NAMES AND TYPE MATERIALS

The two new minerals paqueite (IMA 2013-053) and burnettite (IMA 2013-054) have been approved by the Commission on New Minerals, Nomenclature, and Classification of the International Mineralogical Association (Ma, 2013a, 2013b). Burnettite is named in

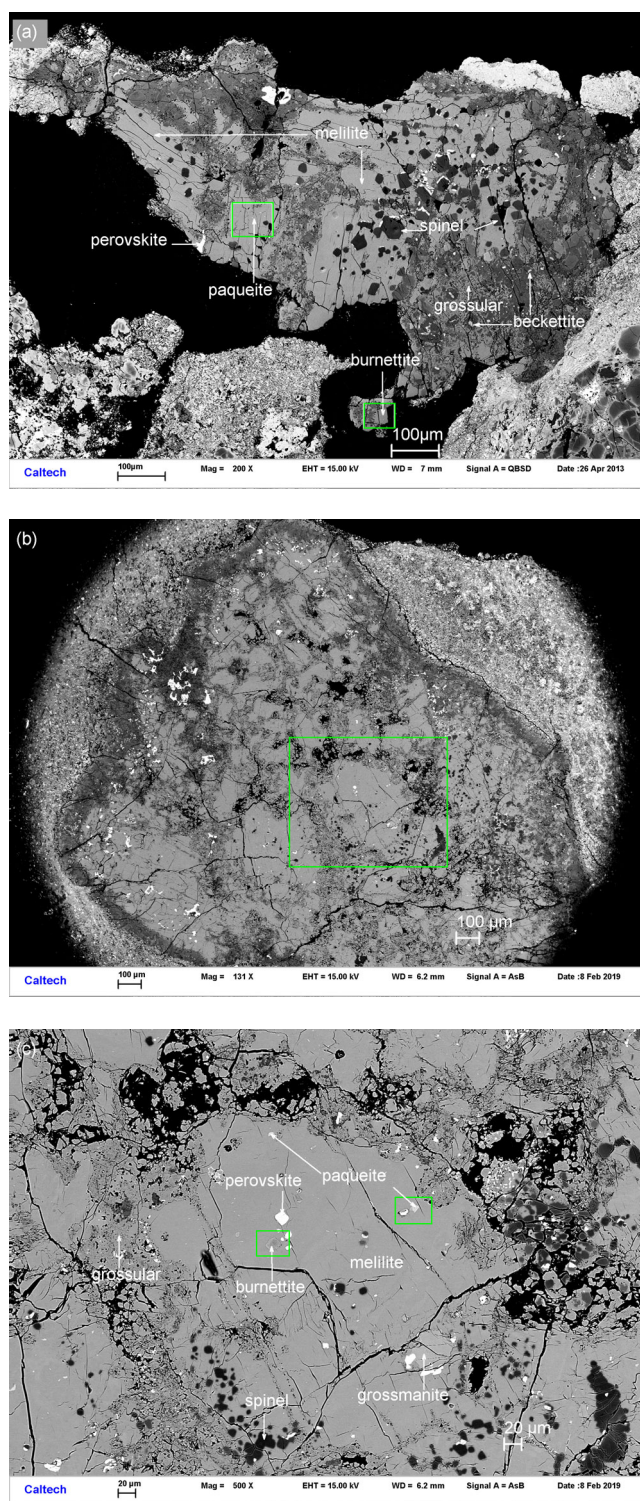


Fig. 1. a) Backscattered electron (BSE) image showing the type A CAI A-WP1 in USNM 7617 and areas containing paqueite and burnettite. b) BSE image of a portion of compact type A *CGft-12*. c) *CGft-12*. Close-up of region outlined by rectangle in (b). Rectangles indicate areas of enlargement shown in Fig. 2. (Color figure can be viewed at [wileyonlinelibrary.com](http://wileyonlinelibrary.com).)

honor of Donald S. Burnett (b. 1937), a cosmochemist at the California Institute of Technology with an extensive publication record on nucleosynthesis, abundances of the elements, trace element analytical techniques, and properties of lunar and meteoritic materials, both through measurements on natural materials and experiments on synthetic analogs (e.g., Burnett, 2006; Burnett et al., 1965, 2015; Burnett & Wasserburg, 1967; Burnett & Woolum, 1977; Connolly & Burnett, 1999; Jones & Burnett, 1987; LaTourette & Burnett, 1992). The name paqueite is in honor of Julie M. Paque (b. 1958), who is also a cosmochemist at the California Institute of Technology. Her work has emphasized analytical and experimental approaches to understanding the nature of CAIs in meteorites (e.g., Paque et al., 1994, 2000, 2009, 2013; Stolper & Paque, 1986). Two of her publications are devoted to the phase that is being named paqueite (Barber et al., 1994; Paque et al., 1994).

Type burnettite occurs in *CGft-12*, an Allende type A inclusion from the Field Museum of Chicago, IL, USA (catalog # ME2639-23.2), not to be confused with the FTA *CG-12*, which was studied by MacPherson and Grossman (1984). *CGft-12* also contains paqueite. Type paqueite occurs within a polished section of Allende in the type A CAI A-WP1, which is deposited under catalog # USNM 7617 in the Smithsonian Institution's National Museum of Natural History, Washington DC, USA. The CAI A-WP1 also hosts the first meteoritic occurrence of baghdadite and the holotype material for a third new mineral, beckettite. The latter phase is described in a companion paper (Ma et al., 2021).

## ANALYTICAL TECHNIQUES

Electron probe microanalysis (EPMA), scanning electron microscopy (SEM), and electron backscatter diffraction (EBSD) were used to characterize chemical compositions and structures of the new minerals and associated phases. EPMA was conducted at the California Institute of Technology on a JEOL 8200 electron microprobe using the Probe for EPMA program from Probe Software, Inc. operated at 10 kV and low beam currents, 5 or 10 nA, in order to minimize activation volumes for the often-tiny grains of interest. Counting times were 20 s on peak and we used the MAN (Donovan & Tingle, 1996) background correction.  $\text{ScPO}_4$  ( $\text{ScK}\alpha$ ), zircon ( $\text{ZrL}\alpha$ ),  $\text{TiO}_2$  ( $\text{TiK}\alpha$ ), anorthite ( $\text{SiK}\alpha$ ,  $\text{AlK}\alpha$ ,  $\text{CaK}\alpha$ ), fayalite ( $\text{FeK}\alpha$ ),  $\text{YPO}_4$  ( $\text{YL}\alpha$ ),  $\text{V}_2\text{O}_5$  ( $\text{VK}\alpha$ ), forsterite ( $\text{MgK}\alpha$ ), and albite ( $\text{NaK}\alpha$ ) were used as standards and analyses were processed using the CITZAF correction procedure of Armstrong (1995). We also obtained backscatter electron images (BSE) and analyzed grains using an



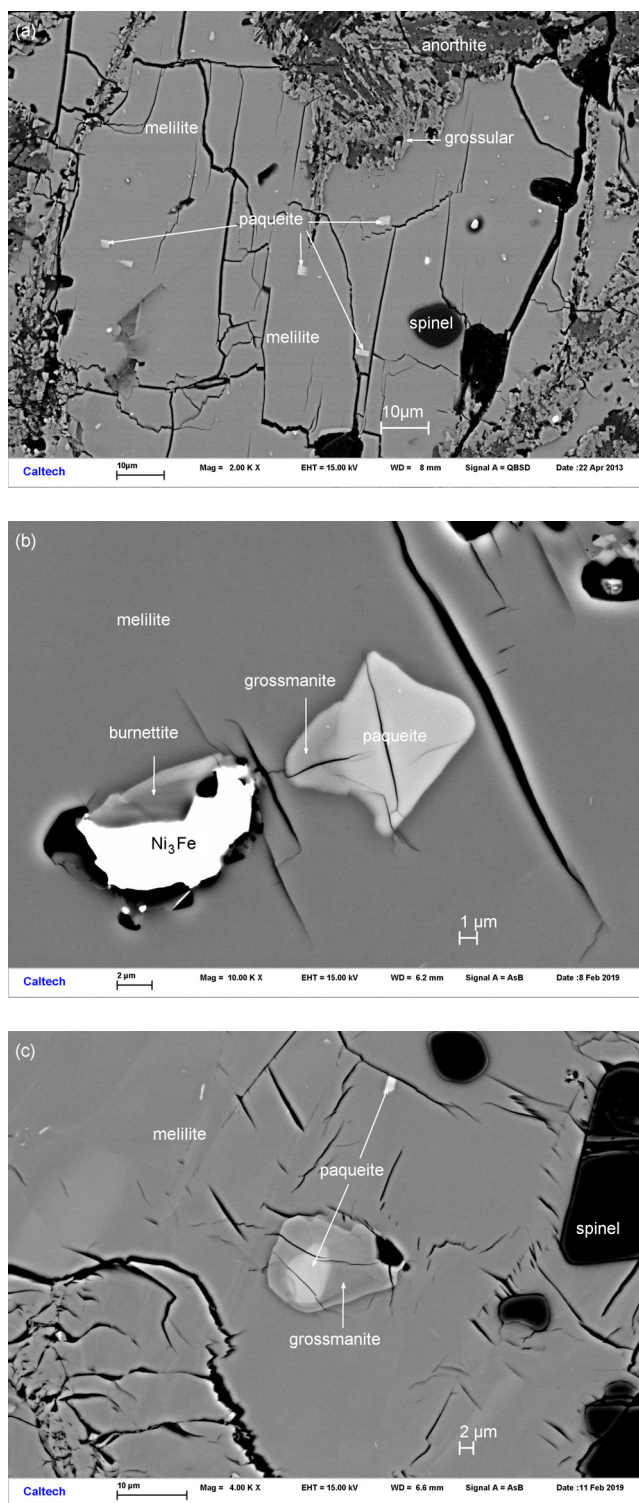


Fig. 2. a) Enlarged BSE image of rectangular region of A-WP1 outlined in Fig. 1a and labeled “paqueite.” b) Close-up view of paqueite and burnettite in *CGft-12*. These grains are in the rectangular outlined regions depicted in Fig. 1c. c) BSE image of paqueite from *CGft-12* included in grossmanite. This is the type paqueite. The image also encompasses an isolated prismatic crystal of paqueite. (Color figure can be viewed at [wileyonlinelibrary.com](http://wileyonlinelibrary.com).)

Oxford INCA X-ray energy-dispersive spectrometer (EDS) mounted on a ZEISS 1550 VP field emission SEM with data processed using the XPP correction procedure of Pouchou and Pichoir (1991) and Oxford factory internal standards. EBSD was also conducted on the SEM using an HKL (now Oxford) EBSD system. The thin sections of A-WP1 and *CGft-12* were vibro-polished and the SEM operated at 20 kV and 4 nA for these measurements, with a focused beam, a 70° tilt, and in variable pressure mode. This approach allowed the use of uncoated samples. The EBSD system was calibrated using a single-crystal silicon standard. Methods used for EBSD are described in detail by Ma and Rossman (2008, 2009b). Micro-Raman analysis was carried out with a Renishaw inVia™ Qontor Raman microscope using a green laser (514 nm) averaging five scans at ~1.0 mW power on the sample in a confocal mode with a 100× objective lens. In all cases, samples were analyzed in random orientation.

## RESULTS

### Occurrence and Appearance

The Allende meteorite fell in and near Pueblito de Allende, Chihuahua, Mexico, on February 8, 1969 (Clarke et al., 1971). This CV3 carbonaceous chondrite is probably the most heavily studied meteorite in existence and results of these studies have greatly influenced current thinking about processes, timing, and chemistry in the primitive solar nebula and in small planetary bodies. Allende continues to be a source of new information on materials produced in the early solar system. For example, paqueite and burnettite are just 2 of 19 new minerals discovered in Allende since 2007 (e.g., Ma, 2015; Ma et al., 2020, 2021).

All of the new minerals occur in A-WP1, an ~800 × 1200 μm fragment of a highly altered, coarse-grained, melilite-rich type A inclusion (Fig. 1a). Large grains (100–300 μm across) of patchily zoned aluminous melilite (mole% åkermanite, Ak8-19) contain included spinel (up to 50 μm across) and sparse perovskite, decorating spinel or as isolated inclusions, along with rare hibonite and refractory metal nuggets. Paqueite occurs in A-WP1 as euhedral to subhedral single crystals, 0.5–2 μm in size, included in melilite (Fig. 2). A-WP1 was an attractive target for study by early workers because it contained V-rich phases. Spinel (1.7–5.4 wt% V<sub>2</sub>O<sub>3</sub>) and hibonite (0.5–1.8 wt% V<sub>2</sub>O<sub>3</sub>) are present and coulsonite (FeV<sub>2</sub>O<sub>4</sub>) occurs as an exsolution phase within V-, Mg-rich hercynite, which is found in heavily altered regions of the inclusion. One isolated grain of baghdadite (Ca<sub>3</sub>[Zr,Ti]Si<sub>2</sub>O<sub>9</sub>) is present. Paque (1989) also reported V-rich alloys in A-WP1. These

analyses were likely contaminated by very small associated V-rich clinopyroxenes, but reported compositions of alloys in Paque (1989) are consistent with those obtained in this study, if the reported V is ignored. Although some phases in A-WP1 and *CGft-12* are extremely V-rich, the phase chemistries are often typical of type As. In particular, spinel and hibonite from other type As can show comparable V contents (see below), so some conclusions regarding A-WP1 and *CGft-12* are likely applicable more generally to type A CAIs and the V-rich phases provide a potential new portal into processes in the early solar system.

Paqueite and burnettite, including the type burnettite, occur in the CTA *CGft-12*. This inclusion (Fig. 1b) is  $8 \times 3$  mm in section and consists of large, partially altered melilite crystals (Ak13-45) with subordinate included grains. In A-WP1, burnettite occurs as one euhedral crystal, 2  $\mu$ m in size (Fig. 3a). It is more common and larger (3–16  $\mu$ m) in *CGft-12* (Fig. 3b). Baghdadite was not observed in *CGft-12*, but spinel, perovskite, davisite, grossmanite, hibonite, and rare Ni-rich ( $\text{Ni}_{0.68}\text{Fe}_{0.30}\text{Co}_{0.02}$ ) and Ru-Os-Fe-Ir-enriched ( $\text{Ru}_{0.48}\text{Os}_{0.27}\text{Fe}_{0.18}\text{Ir}_{0.03}\text{Ni}_{0.02}$ ) alloys were.

As part of this study, we also examined two Allende FTAs, *ALH1* and *TS-28*, from the Field Museum collection. These inclusions were previously studied by MacPherson and Grossman (1984) and Simon et al. (2001), respectively. Neither of these FTAs was found to contain any of the new minerals described in this work or in Ma et al. (2021), although *ALH1* does contain V-bearing grossmanite (up to 2.0 wt%  $\text{V}_2\text{O}_3$ ).

For many new minerals, the initial description of the named mineral also provides the first known occurrence. Paqueite, however, has a history. Allen et al. (1978) noted the presence of fine needles of a phase with a roughly square cross section that may have been paqueite. They did not attempt to characterize the chemistry but noted that the phase occurred sparsely in the FTA *CG-11* and “in other coarse-grained Allende inclusions.” They also noted that the phase frequently aligned parallel or perpendicular to the (001) cleavage of host melilite and inferred that it was an exsolution product. El Goresy et al. (1984) described a likely grain of paqueite in melilite within a compound collection of mostly hibonite–spinel spherules. Their grain had significant concentrations of the heavy rare earth elements (REE; 0.1–0.3 wt%) and established the occurrence of this phase outside that of coarse-grained inclusions (i.e., this phase was unlikely to have been an exsolution product of melilite), although it retains a strong association of paqueite with melilite. Paque et al. (1994) described likely paqueite in a variety of type A (coarse-grained; melilite-dominant) and type

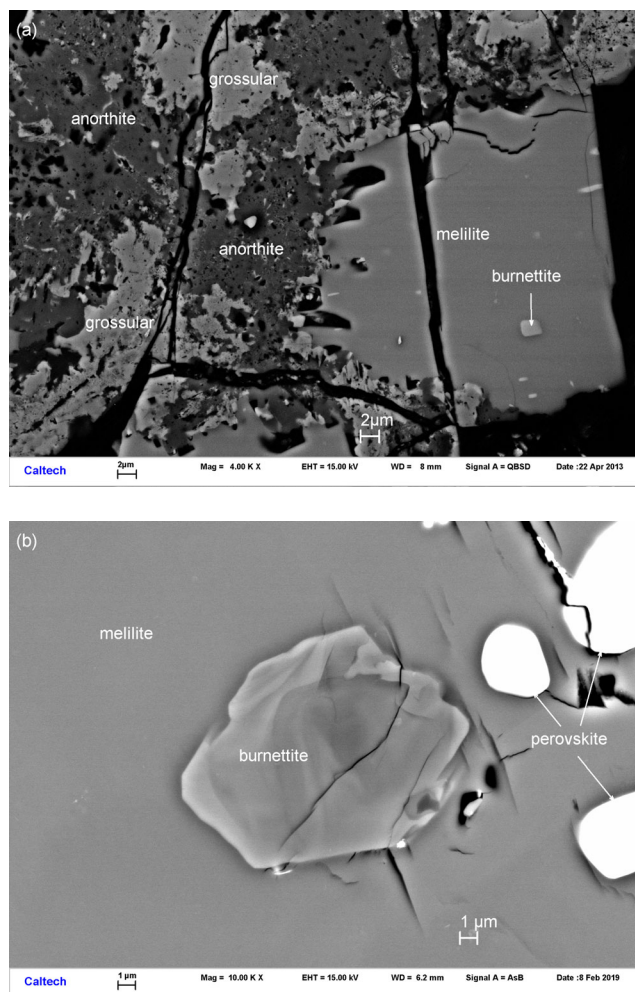


Fig. 3. BSE images showing burnettite. a) Area of A-WP1 enclosed in rectangle in Fig. 1a showing general petrographic context for this grain. b) Enlarged BSE image of the type burnettite grain from *CGft-12*. The general petrographic context for this grain is shown in Fig. 1c within the area labeled “burnettite.” (Color figure can be viewed at [wileyonlinelibrary.com](http://wileyonlinelibrary.com).)

B (coarse-grained; subequal amounts of melilite,  $\text{Ti}^{3+}$ -bearing clinopyroxene, and  $\text{MgAl}_2\text{O}_4$  spinel) CAIs, including A-WP1. The grains of likely paqueite were invariably enclosed in melilite. Caillet Komorowski et al. (2007) observed likely paqueite in melilite in *White Angel*, an FTA from Leoville (CV3). The various modes of occurrence are consistent with, but do not require, more than one mode of origin (e.g., exsolution, condensation, crystallization from a melt). There is nevertheless a universal association of paqueite with melilite in meteoritic occurrences. Paqueite has also been reported in a variety of synthetic systems, most notably in cooling rate experiments on CAI-like bulk compositions conducted at 1 atm and in a slag (Barber & Agrell, 1994; Barber et al., 1994; Beckett & Stolper,

1994). However, Scheuermann et al. (2000) also produced paqueite at 1.5 GPa in experiments on the system  $\text{Ca}_2\text{Al}_2\text{Si}_2\text{O}_8\text{-CaTiSiO}_5$  (i.e., anorthite–titanite) where no melilite was present. These experimental results suggest that paqueite has a broad range of stability, or at least metastability, in terms of bulk composition, pressure, and temperature.

Burnettite occurs as a single isolated 2  $\mu\text{m}$  crystal enclosed in melilite in A-WP1 (Fig. 3a) and as multiple grains, up to 15  $\mu\text{m}$  across, in *CGft-12* (Fig. 3b). The only previously described meteoritic pyroxenes with high concentrations of V that we are aware of (9.0–10.3 wt%  $\text{V}_2\text{O}_3$ ) occur as rims on an opaque assemblage in an Allende igneous CAI (Armstrong et al., 1985).  $\text{V}_2\text{O}_3$  contents of the Armstrong et al. (1985) clinopyroxenes are within the range observed for burnettite in this study (9.2–9.5 wt%  $\text{V}_2\text{O}_3$  for A-WP1 and 11.5–18.8 wt%  $\text{V}_2\text{O}_3$  for *CGft-12*). However, Mg is the dominant octahedral cation in these clinopyroxenes. Thus, in spite of their very high concentrations of V, the clinopyroxenes of Armstrong et al. (1985) are V-rich diopsides and not burnettites.

### Physical and Optical Properties

Color, luster, streak, hardness, tenacity, cleavage, fracture, density, and optical properties of paqueite and burnettite were not determined experimentally because of the small grain sizes or because the available section was optically thick. For burnettite, these properties are likely to be similar to those of synthetic burnettite (Taran & Ohashi, 2012) and other synthetic and natural Ca-clinopyroxenes. Neither burnettite nor paqueite shows cathodoluminescence under the electron beam. The densities, calculated from their crystal structures and the empirical formulas, as described below, are 3.39  $\text{g cm}^{-3}$  for paqueite from A-WP1 and 3.44  $\text{g cm}^{-3}$  for burnettite from *CGft-12*. Scheuermann et al. (2000) obtained a higher density, 4.01  $\text{g cm}^{-3}$ , for paqueite synthesized at 1.5 GPa.

### Spectroscopy

Raman spectra of paqueite, burnettite, and adjacent melilite crystals in *CGft-12* are shown in Fig. 4 (spectra of the much smaller grains of both burnettite and paqueite in A-WP1 were completely dominated by melilite spectral components superimposed upon a strong, underlying broad fluorescence). A modest baseline correction to remove background curvature was performed on the melilite prior to its presentation. Peak positions of the prominent bands in the spectra of burnettite, paqueite, and melilite are labeled. In the spectra of both burnettite and paqueite, minor features

marked by asterisks indicate contributions from the host melilite (compare with the melilite spectrum). Also shown in Fig. 4 is a comparison of the burnettite spectrum to the spectra of two other meteoritic clinopyroxenes from CAIs with M1 sites dominated by trivalent cations, namely, davisite (ideally,  $\text{CaScAlSiO}_6$ ) and grossmanite (ideally,  $\text{CaTi}^{3+}\text{AlSiO}_6$ ). These were taken from Ma and Rossman (2009a, 2009c), respectively. There is an appreciable degree of similarity of the spectrum of burnettite to that of grossmanite. Similar features can also be seen in the spectrum for davisite, although there appears to be contamination in the observed davisite spectrum from other phases.

### Crystallography

For each new mineral, the structure was determined and cell constants obtained by matching the experimental EBSD patterns with calculated patterns defined by related structures. Analytical procedures are described above. In this section, we describe the results of the EBSD measurements and give brief descriptions of the structures for two of the new minerals, paqueite and burnettite, and consider how the structures might impact the crystal chemistry.

EBSD patterns of paqueite match only to the *P321* trigonal structure of synthetic  $\text{Ca}_3\text{TiSi}_2(\text{Al,Ti,Si})_3\text{O}_{14}$  from Scheuermann et al. (2000), with a mean angular deviation of  $0.46^\circ$ , showing  $a = 7.943 \text{ \AA}$ ,  $c = 4.930 \text{ \AA}$ ,  $V = 269.37 \text{ \AA}^3$ , and  $Z = 1$  (Fig. 5a). The structure consists of a tetrahedral layer perpendicular to [001] with two distinct tetrahedral sites, one occupied solely by Si and the other, larger, site containing a mixture of Si, Al, and Ti. This layer alternates with octahedral layers containing mostly Ti. Due to their relatively large size, it is expected that  $\text{Ti}^{3+}$  and  $\text{V}^{3+}$ , if present, would substitute predominately into the octahedral site (i.e., essentially all Ti in the tetrahedral site is quadrivalent). Calcium is located in eight distorted coordinated sites dictated by the tetrahedral layer and large ion lithophiles, like the REE, will also likely substitute into these sites. For the trivalent REE, charge balancing paired substitutions (or defects) would be required. Paqueite is not structurally related to other minerals (i.e., it would be the founding and only member of a paqueite group), but there are hundreds of known synthetic *P321* germanates and langasites that are isotypic with paqueite (e.g., Kaminskii et al., 1984; Mill' et al., 1983; Reinhardt et al., 2018). These materials are important potential laser and light emitting diode phosphors and find use as acoustic wave filters and electro-optic Q-switches. Most were synthesized in air at elevated temperatures and ambient pressure. However, Gasparik et al. (1995) described an isotypic phase with



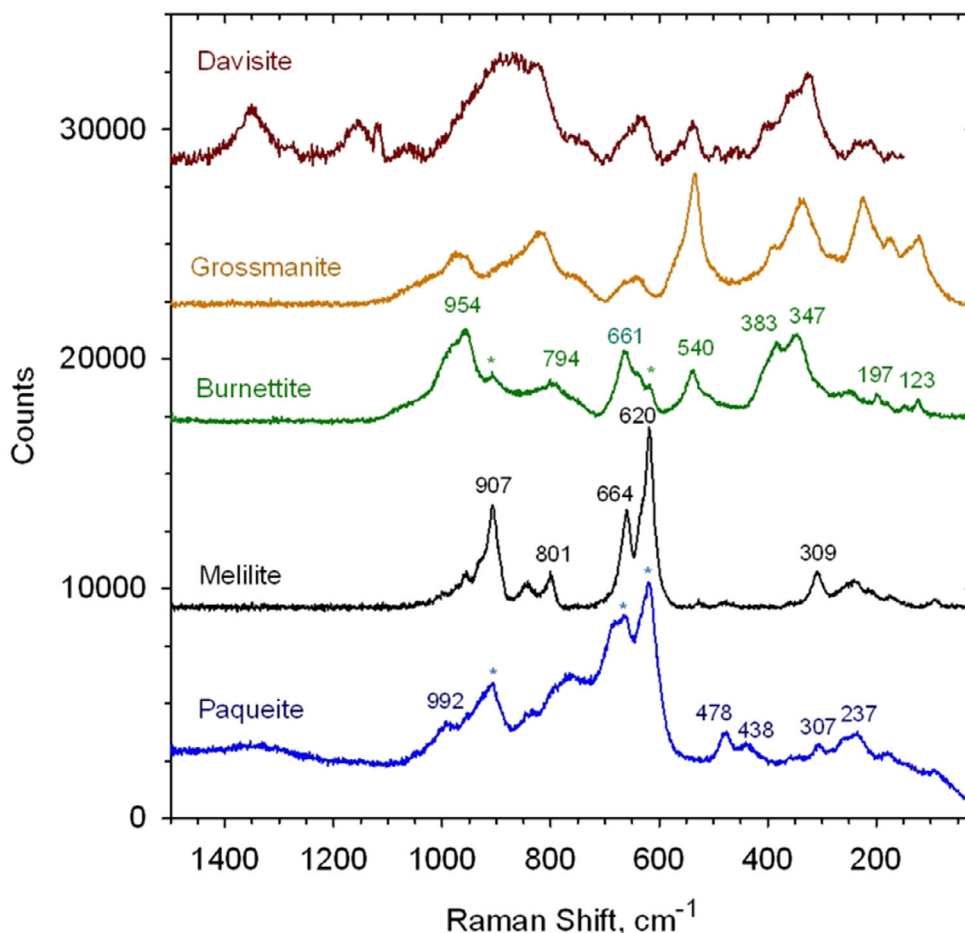


Fig. 4. Raman spectra of the type paqueite and burnettite in *CGft-12* compared to melilite in *CGft-12* and the meteoritic pyroxenes, davisite, and grossmanite, taken from Ma and Rossman (2009a) and Ma and Rossman (2009c), respectively. (Color figure can be viewed at [wileyonlinelibrary.com](http://wileyonlinelibrary.com).)

a formula of  $\text{Na}_{1.8}\text{Ca}_{1.1}\text{Si}_6\text{O}_{14}$ , which crystallized at 8–15 GPa, and, as noted above, Scheuermann et al. (2000) synthesized paqueite at 1.5 GPa.

The EBSD patterns of burnettite (Fig. 5b) can only be indexed by a  $C2/c$  diopside-type structure and we obtained a best fit using the cell parameters for a  $\text{Ti}^{3+}$ -bearing diopside taken from the structure refinement of a type B Allende CAI (Dowty & Clark, 1973), with a mean angular deviation of  $0.45^\circ$ , and cell parameters  $a = 9.80 \text{ \AA}$ ,  $b = 8.85 \text{ \AA}$ ,  $c = 5.36 \text{ \AA}$ ,  $\beta = 105.62^\circ$ , with  $V = 447.70 \text{ \AA}^3$  and  $Z = 4$ . The  $C2/c$  clinopyroxenes are major rock-forming minerals (e.g., Deer et al., 1992). They are chain silicates but can also be thought of as consisting of alternating tetrahedral and octahedral layers parallel to (001). The reader is referred to Cameron and Papike (1981) for a detailed description. To zeroth order, the partitioning behavior for trace elements between burnettite and other phases is likely to be similar to that of  $\text{Ti}^{3+}$ -bearing clinopyroxenes from type B inclusions (e.g., Simon et al., 1991). If so,

relative to a CAI-like melt, Sc,  $\text{V}^{3+}$ , and  $\text{Ti}^{3+}$  would be strongly compatible in burnettite; Hf and  $\text{Ti}^{4+}$ , slightly compatible or slightly incompatible; and Zr, Y, Ta, and the REE, incompatible.

X-ray powder diffraction data (Tables S1 and S2 in supporting information, in  $\text{Å}$  for  $\text{CuK}\alpha_1$ , Bragg-Brentano geometry) for paqueite and burnettite from A-WP1 were calculated from the above cell parameters and the empirical formula from this work, using Powder Cell version 2.4.

### Chemical Composition

EPMA analyses of paqueite, burnettite, and other phases from A-WP1 and *CGft-12* are given in Tables 1 and 2. In this section, we consider the empirical formulas for paqueite and burnettite and how these formulas relate to nomenclature. We include Ti-, Sc-enriched clinopyroxenes along with burnettite and V-rich kushiroites in this section, but compositions of

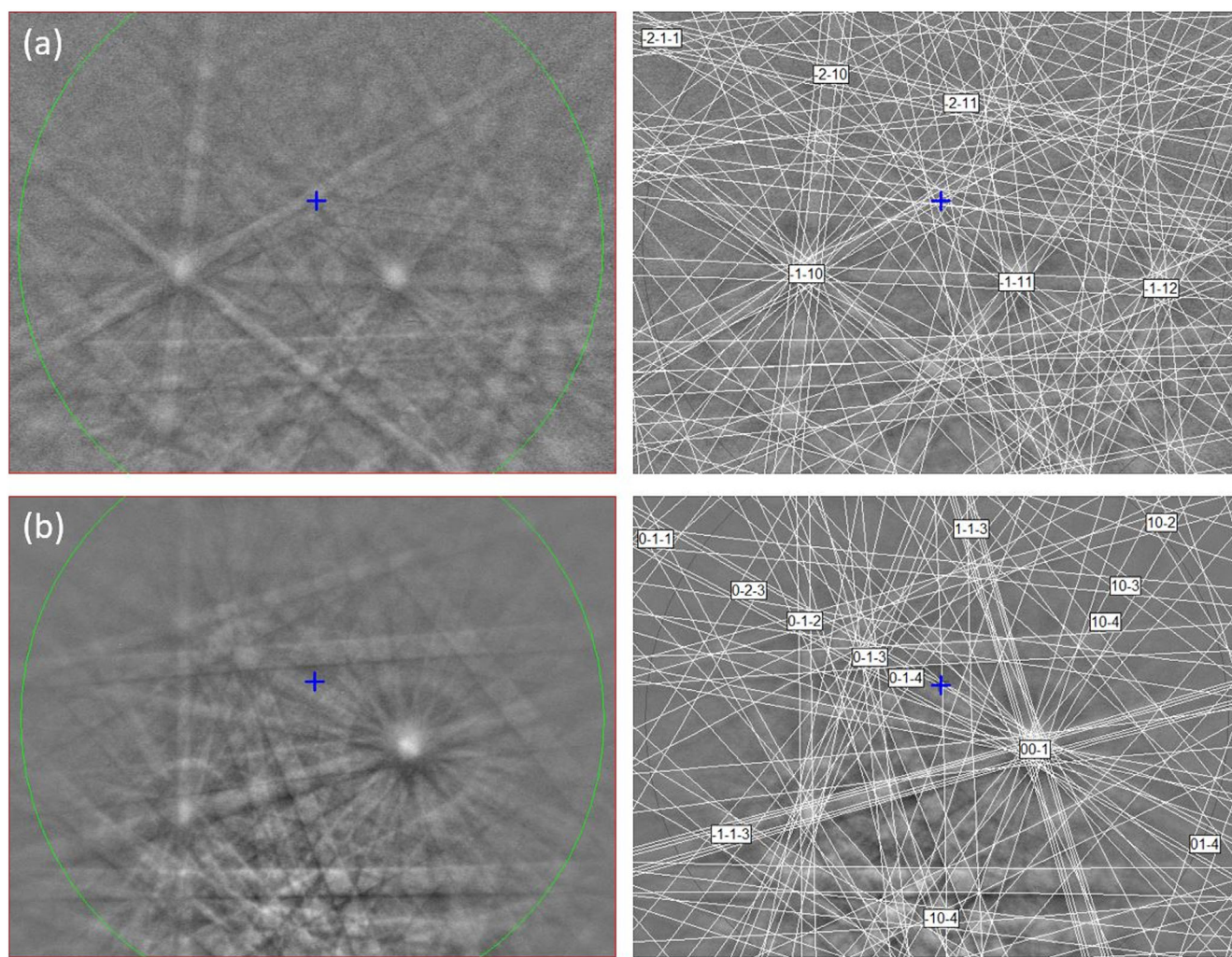


Fig. 5. EBSD patterns of the new minerals. For each mineral, the EBSD pattern is shown in the left-hand panel and the indexed pattern in the right-hand panel. The center of each pattern is indicated by a cross. a) EBSD pattern of the type paqueite crystal shown in Fig. 2a, indexed with the  $P321$  trigonal structure of Scheurmann et al. (2000). b) EBSD pattern of the type burnettite crystal shown in Fig. 3b, indexed with the  $C2/c$  pyroxene structure of Dowty and Clark (1973). (Color figure can be viewed at [wileyonlinelibrary.com](http://wileyonlinelibrary.com).)

other phases are considered in the following section on coexisting phases or in Ma (2018) and Ma et al. (2021). It should always be kept in mind that mineral name designations within solid solutions, such as  $C2/c$  clinopyroxenes, carve out arbitrary boundaries (i.e., the mineral names are fundamentally semantic, not genetic).

### *Paqueite*

The type paqueite in *CGft-12* (Fig. 2c) shows an empirical formula (based on 14 O *apfu*) of  $\text{Ca}_{2.95}\text{TiSi}_2(\text{Al}_{1.60}\text{Ti}^{4+}_{0.55}\text{Si}_{0.40}\text{V}^{3+}_{0.32}\text{Ti}^{3+}_{0.13}\text{Mg}_{0.02}\text{Sc}_{0.01}\text{Zr}_{0.01})\text{O}_{14}$ . The general formula is  $\text{Ca}_3\text{TiSi}_2(\text{Al},\text{Ti},\text{Si})_3\text{O}_{14}$  and the endmember formula is  $\text{Ca}_3\text{TiSi}_2(\text{Al}_2\text{Ti})\text{O}_{14}$ . Most meteoritic and synthetic paqueites are approximately

binary solutions of  $\text{Ca}_3\text{Ti}^{4+}\text{Si}_2\text{Al}_2\text{Ti}^{4+}\text{O}_{14}$  (i.e., endmember paqueite) and  $\text{Ca}_3\text{Al}_2\text{Si}_4\text{O}_{14}$  with, typically, up to a few mole% each of  $\text{Ti}^{3+}$ ,  $\text{V}^{3+}$ , and Mg-bearing components. Based on the analysis reported by El Goresy et al. (1984), the phase can also contain several tenths of a wt% of the heavy REE. Thus, as noted by Paque and Stolper (1984), variations in the major element chemistry of paqueite can be described, to zeroth order, in terms of variations in the concentrations of Si and Ti. In Fig. 6a, cations of  $\text{Ti}^{4+}$ , where Ti valence was computed assuming a stoichiometric paqueite with nine cations and 14 oxygen anions, are plotted as a function of Si in meteoritic and synthetic paqueite. Synthetic paqueites cover a much broader range in composition, with one grain analyzed by Paque et al. (1994) approaching that of endmember  $\text{Ca}_3\text{Al}_2\text{Si}_4\text{O}_{14}$ . Note



Table 1. EPMA data for burnettite, paqueite, and associated phases in A-WP1.

Constituent wt%	Burnettite		Melilite <sup>a</sup>		Paqueite		Melilite <sup>c</sup>		Davisite		Spinel		Hibonite		Perovskite	
	<i>n</i> = 5	SD	<i>n</i> = 3	SD <sup>b</sup>	<i>n</i> = 5	SD	<i>n</i> = 6	SD	<i>n</i> = 3	SD	<i>n</i> = 3	SD	<i>n</i> = 4	SD	<i>n</i> = 6	SD
SiO <sub>2</sub>	25.69	0.33	23.93	0.23	24.43	0.32	24.76	0.63	25.01	0.06	0.22	0.06	0.49	0.14	0.44	0.31
TiO <sub>2</sub> <sup>d</sup>	4.30	0.10	b.d. <sup>e</sup>		27.51	0.26	b.d.		6.63	0.59	0.18	0.08	3.05	1.33	54.81	0.24
Ti <sub>2</sub> O <sub>3</sub> <sup>d</sup>	3.77								4.70							
Al <sub>2</sub> O <sub>3</sub>	23.37	0.13	33.33	0.48	15.21	0.63	31.95	1.17	24.20	0.35	68.69	0.15	85.00	2.17	0.66	0.12
FeO	b.d.		b.d.		b.d.		b.d.		b.d.		1.12	0.17	0.19	0.04	b.d.	
MgO	1.51	0.08	1.28	0.08	0.18	0.06	1.88	0.30	1.65	0.04	26.44	0.21	1.66	0.65	b.d.	
CaO	24.83	0.10	40.09	0.11	29.58	0.36	40.89	0.82	25.49	0.27	0.26	0.00	8.39	0.05	39.45	0.22
Na <sub>2</sub> O	b.d.		b.d.		0.62	0.03	0.05	0.06	0.05	0.01	b.d.		0.05	0.04	b.d.	
V <sub>2</sub> O <sub>3</sub>	9.35	0.08	b.d.		1.56	0.21	b.d.		5.27	0.23	1.70	0.06	0.59	0.10	4.79	0.15
Sc <sub>2</sub> O <sub>3</sub>	6.89	0.17	b.d.		0.84	0.17	b.d.		7.71	0.67	b.d.		b.d.		0.15	0.07
ZrO <sub>2</sub>	b.d.		b.d.				b.d.				b.d.		b.d.		0.30	0.28
Total	99.71		98.63		99.92		99.53		100.71		98.59		99.44		100.60	
No. O atoms	6		7		14		7		6		4		19		3	
Si	1.01		1.10		2.24		1.13		0.97		0.01		0.06		0.01	
Ti <sup>4+</sup>	0.13				1.90				0.19		0.00		0.26		0.93	
Ti <sup>3+</sup>	0.12								0.15							
Al	1.08		1.81		1.64		1.74		1.10		1.96		11.31		0.02	
Fe											0.02		0.02			
Mg	0.09		0.09		0.02		0.12		0.10		0.96		0.28			
Ca	1.04		1.98		2.91		2.01		1.06		0.01		1.02		0.95	
Na					0.11		0.00		0.00				0.01			
V <sup>3+</sup>	0.29				0.11				0.16		0.03		0.05		0.09	
Sc	0.24				0.07				0.26						0.00	
Zr															0.00	
Cation sum	4.00		4.98		9.00		5.00		4.00		2.99		13.00		2.00	

<sup>a</sup>Near burnettite.<sup>b</sup>One standard deviation of the mean for all of the cited analyses.<sup>c</sup>Near paqueite.<sup>d</sup>Ti partitioned between TiO<sub>2</sub> and Ti<sub>2</sub>O<sub>3</sub> via stoichiometry (see text).<sup>e</sup>b.d. = below detection limit, Na 0.03 wt%, Ti 0.06 wt%, Fe 0.16 wt%, V 0.04 wt%, Sc 0.03 wt%.

that there is a substantial gap in composition between Ti-rich paqueites and Ca<sub>3</sub>Al<sub>2</sub>Si<sub>4</sub>O<sub>14</sub> (Fig. 6a). Given that the structure of the Si-endmember could be different from that of paqueite, the extraordinarily Si-rich phase may reflect a miscibility gap (i.e., paqueites with intermediate compositions are unstable at accessible temperatures), but it is also possible that such Si-rich paqueites are stable but existing experiments and samples from characterized natural environments have not accessed the conditions and/or bulk compositions required to produce it.

Paqueites contain a variety of minor elements that can potentially help constrain the nature of the environments in which they formed. Ratios of multivalent cations such as V and Ti are sensitive to redox conditions. Neither V<sup>2+</sup>/V<sup>3+</sup> nor Ti<sup>3+</sup>/Ti<sup>4+</sup> content of paqueites have been measured directly. However, assuming a stoichiometric formula with nine cations per 14 oxygens, 0–13% of the Ti in paqueites from *CGft-12* and A-WP1 is trivalent, consistent with calculations of Paque et al. (1994) for paqueite from a wide variety of CAIs. Calculated Ti<sup>3+</sup>/Ti<sup>4+</sup> is

proportional to the Ti<sup>3+</sup> content because the concentrations of Ti<sup>4+</sup> ≫ Ti<sup>3+</sup>, but we noted no general correlation with V, which might be expected if calculated Ti<sup>3+</sup> was an artifact of V<sup>2+</sup> being ignored. It is also important to note that the inferred Ti<sup>3+</sup>/Ti<sup>4+</sup> for paqueite is much lower than in adjacent grossmanite. For the grossmanite–paqueite pair shown in Fig. 2c, Ti<sup>3+</sup>/Ti<sup>4+</sup> is 0.04–0.11 in the paqueite compared to 0.5–4.1 in the grossmanite. This is not entirely a reflection of tetrahedral Ti<sup>4+</sup> in paqueite distorting the calculated Ti<sup>3+</sup>/Ti<sup>4+</sup> ratio. If it is assumed that only octahedral Ti is reducible, then (Ti<sup>3+</sup>/Ti<sup>4+</sup>)<sub>oct</sub>, where the subscript “oct” refers to octahedral sites in the large paqueite grain shown in Fig. 2c, is 0.11–0.25, still considerably less than in coexisting grossmanite. Ratios among the analyzed paqueites in A-WP1 and *CGft-12* are as high as 0.75, but these are still only at the lower end of values for grossmanite from the same inclusions.

Paqueite grains from A-WP1 and *CGft-12* have 0.01–0.08 cations of Sc, 0.06–0.33 cations of V, and 0.01–0.22 cations of Mg pfu. For the latter, most

Table 2. Compositions of phases in *CGft-12*.

Oxide wt%	Burnettite		Mellilite <sup>a</sup>		Paquite		Mellilite <sup>b</sup>		Grossmanite		Davisite		Spinel		Perovskite		Hibonite	
	n = 6	SD <sup>c</sup>	n = 8	SD	n = 8	SD	n = 7	SD	n = 14	SD	n = 8	SD	n = 6	SD	n = 6	SD	n = 8	SD
SiO <sub>2</sub>	30.52	0.75	27.61	0.38	26.11	0.26	29.59	0.50	28.46	0.46	27.85	0.27	b.d. <sup>d</sup>	b.d. <sup>d</sup>	0.17	0.09	0.10	0.06
TiO <sub>2</sub> <sup>e</sup>	0.11	0.07	b.d.		22.45	0.43	b.d.		4.34	0.28			0.17	0.01	56.47	0.39	6.26	1.14
Ti <sub>2</sub> O <sub>3</sub> <sup>e</sup>					1.63	0.03			14.78	0.96	5.65	0.55						
Al <sub>2</sub> O <sub>3</sub>	23.06	1.20	27.20	0.67	14.77	0.21	24.25	1.03	21.06	0.73	20.84	0.40	69.48	0.33	0.19	0.03	80.55	1.94
FeO	0.11	0.05	0.07	0.04	b.d.		0.17	0.04	b.d.		b.d.		0.32	0.21	b.d.	b.d.	b.d.	
MgO	3.09	0.46	3.68	0.25	0.16	0.03	4.73	0.35	4.10	0.15	2.08	0.27	27.80	0.16	b.d.		3.19	0.60
CaO	24.18	0.61	41.04	0.35	29.90	0.32	40.59	0.28	24.01	0.60	23.45	0.34	0.24	0.06	39.94	0.28	8.25	0.16
V <sub>2</sub> O <sub>3</sub>	17.91	1.48	b.d.		4.33	0.10	b.d.		2.97	0.67	7.79	0.23	1.48	0.18	3.27	1.96	1.49	0.15
Sc <sub>2</sub> O <sub>3</sub>	0.03	0.03	0.04	0.03	0.18	0.04	0.04	0.02	0.44	0.15	11.26	1.13	b.d.		0.08	0.05	0.06	0.05
ZrO <sub>2</sub>	b.d.		b.d.		0.28	0.08	b.d.		0.25	0.17	1.33	0.16	b.d.		0.22	0.09	b.d.	
Y <sub>2</sub> O <sub>3</sub>	0.03	0.03	b.d.		b.d.		b.d.		b.d.		b.d.		b.d.		0.16	0.07	b.d.	
Total	99.04		99.61		99.80		99.37		100.40		100.25		99.48		100.49		99.91	
No. O atoms	6		7		14		7		6		6		4		3		19	
Si	1.19		1.26		2.40		1.35		1.10		1.09		0.00		0.00		0.01	
Ti <sup>4+</sup>	0.00				1.55				0.13				0.00		0.96		0.53	
Ti <sup>3+</sup>					0.13				0.48		0.18							
Al	1.06		1.47		1.60		1.31		0.96		0.96		1.96		0.00		10.76	
Fe	0.00		0.00				0.01						0.01					
Mg	0.18		0.25		0.02		0.32		0.24		0.12		0.99				0.54	
Ca	1.01		2.01		2.95		1.99		0.99		0.98		0.01		0.97		1.00	
V	0.56				0.32				0.09		0.24		0.03		0.06		0.14	
Sc	0.00		0.00		0.01		0.00		0.01		0.38				0.00		0.01	
Zr					0.01				0.00		0.03				0.00		0.00	
Y	0.00														0.00		0.00	
Cation sum	4.00		5.00		9.00		4.99		4.00		4.00		3.00		2.00		13.00	

<sup>a</sup>Next to burnettite.<sup>b</sup>Next to paquite.<sup>c</sup>One standard deviation of the mean for all of the cited analyses.<sup>d</sup>b.d. = below detection limit, Na 0.03 wt%, Ti 0.06 wt%, Fe 0.16 wt%, V 0.04 wt%, Sc 0.03 wt%.<sup>e</sup>Ti partitioned between TiO<sub>2</sub> and Ti<sub>2</sub>O<sub>3</sub> via stoichiometry (see text).



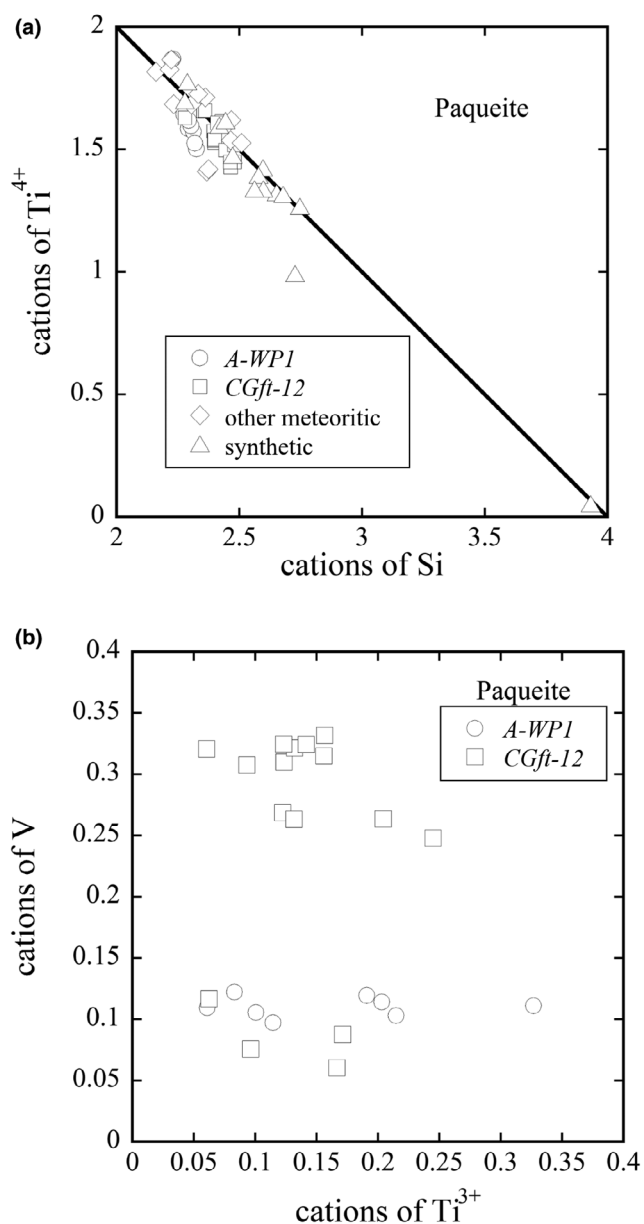


Fig. 6. a) Cations of Si versus cations of  $\text{Ti}^{4+}$  pfu with 14 oxygens in meteoritic and synthetic paqueite. Data are from Barber and Agrell (1994), Beckett and Stolper (1994), Caillet Komorowski et al. (2007), El Goresy et al. (1984), Krot et al. (2007), Paque et al. (1994), and this study. b) Cations of  $\text{Ti}^{3+}$  in paqueite from *A-WP1* and *CGft-12* versus cations of V.

analyses have only 0.02–0.04 cations of Mg pfu but one grain (Fig. 2c), which is surrounded by grossmanite, displays much higher concentrations (0.03–0.22) and may be an indicator for paqueite crystallized from relatively late-stage magnesian melts or equilibrated with an Mg-rich system. Vanadium concentrations are bimodal (Fig. 6b). All of the paqueites in *A-WP1* have ~0.1 cations of V pfu, as does the *CGft-12* paqueite

shown in Fig. 2c. If the paqueite shown in Fig. 2c equilibrated with the enclosing grossmanite, the apparent partition coefficient for V,  $D_V^{\text{Gsm}/\text{Paq}} = \text{wt\% V in grossmanite}/\text{wt\% V in paqueite}$ , where “Gsm” refers to grossmanite and “Paq” to paqueite ~2. Other paqueites from *CGft-12* have substantially higher concentrations, 0.24–0.33 cations of V pfu than the grain shown in Fig. 2c.

#### Burnettite and Other Clinopyroxenes

Type burnettite from *CGft-12* (Fig. 3b) has an empirical formula (based on six oxygens and four cations apfu) of  $\text{Ca}_{1.01}(\text{V}^{3+}_{0.56}\text{Al}_{0.25}\text{Mg}_{0.18})(\text{Si}_{1.19}\text{Al}_{0.81})\text{O}_6$ . It is a calcic *C2/c* clinopyroxene with trivalent cations dominant in the octahedral *M1* site and V the dominant trivalent cation. The general formula is  $\text{Ca}(\text{V}, \text{Al}, \text{Mg})\text{AlSiO}_6$  and the endmember formula is  $\text{CaVAlSiO}_6$ . Burnettite is the  $\text{V}^{3+}$ -analog of davisite (Sc dominant in *M1*), kushiroite (Al), essenite ( $\text{Fe}^{3+}$ ), and grossmanite ( $\text{Ti}^{3+}$ ). The assignment of a particular name to a particular clinopyroxene in a type A inclusion is based on the dominant trivalent cation (diopsides, which have Mg as the dominant octahedral cation, occur in the rim regions of *CGft-12*, but these are ignored for present purposes) and this can be any of  $\text{V}^{3+}$  (burnettite), Al (kushiroite), Sc (davisite), or  $\text{Ti}^{3+}$  (grossmanite). The name can change even within a crystal (i.e., the designation represents a semantic binning within a continuum of compositions).

It is important to note that we assumed V to be trivalent in constructing the empirical formula for burnettite. Vanadium can assume a wide variety of valences in crystalline materials, ranging from 0 to 5 (e.g., Wong et al., 1984) and, in particular, Simon et al. (2007) found, using XANES, that about half of the V in  $\text{Ti}^{3+}$ -bearing clinopyroxene within Allende type B inclusions and in Wark–Lovering rims from types A and B inclusions was divalent. They did not measure V valence in burnettites, but their result will clearly not extend to this phase. In Fig. 7, we show cations of  $\text{Mg}+\text{Fe}-\text{Zr}-\text{Ti}^{4+}$  in the *M1* site, a measure of charge available to charge balance Si, for the type burnettite in *CGft-12*. In Fig. 7, all Ti has been computed as  $\text{Ti}^{4+}$ . If all of the V is trivalent and all of the Ti is tetravalent, the data should conform to a line with a slope and *x*-intercept of 1, reflecting the substitution of trivalent cations with molecules of the form  $\text{CaR}^{3+}\text{AlSiO}_6$ , where  $\text{R}^{3+}$  represents an arbitrary trivalent cation. In this case, no divalent cations other than Mg and Fe on the octahedral site and, in particular, no significant concentration of  $\text{V}^{2+}$ , is indicated. Most of the data adhere closely to the 1:1 line in Fig. 7, consistent with there being few, if any, divalent cations other than the observed Mg and Fe being required to account for the

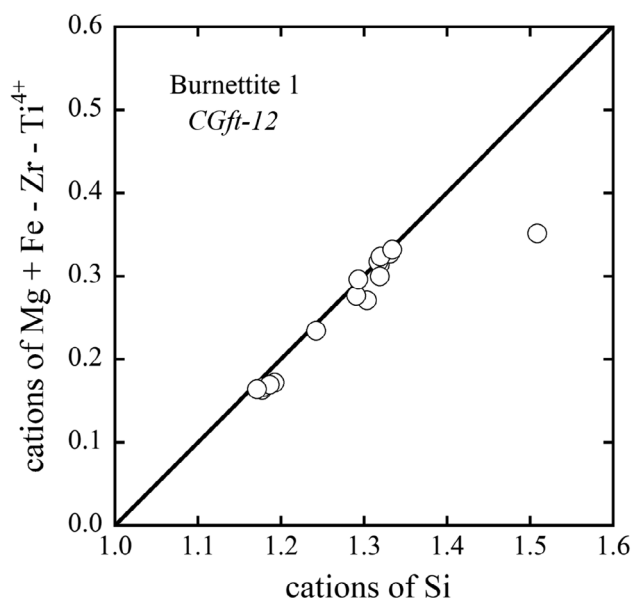


Fig. 7. Cations of Si versus Mg + Fe–Zr–Ti\* (all Ti computed as Ti<sup>4+</sup>) in type burnettite from *CGft-12*.

observed Si content. The modest observed deviations from the line are consistent with the presence of small concentrations of Ti<sup>3+</sup>, which was calculated as Ti<sup>4+</sup>. We, therefore, conclude that V<sup>3+</sup> is the dominant valence for V in the type burnettite. The highest Si point in Fig. 7 is exceptional in plotting well below the 1:1 line. This analysis contains 2.9 wt% Ti computed as TiO<sub>2</sub> (versus 0.1–1.1 wt% for the other analyses), but even this additional Ti is insufficient to account for most of the discrepancy and the stoichiometry is consistent with no contamination from adjacent melilite. A simple explanation for this datum is the presence of significant concentrations of V<sup>2+</sup>. Since this analysis is from the rim of the type burnettite, it suggests that there may have been a reduction event late in the growth of this crystal.

In the above paragraph, we emphasized V concentration and valence because these are critical in defining the new mineral burnettite. By name, however, there are multiple types of clinopyroxene in A-WP1 and *CGft-12* (burnettite, davisite, grossmanite, kushiroite; also, diopside, although we are generally ignoring that phase in this work), reflecting a broad range in composition. It is by considering all of the clinopyroxenes together that genetic information is most likely to be found. Figure 8 shows compositions of clinopyroxenes in *CGft-12* and A-WP1, with associated mineral names for the former and a generic clinopyroxene designation for the latter. Consider first the davisite–grossmanite clinopyroxenes from *CGft-12*. In Fig. 8a, the Sc-rich members of this grouping (>6 wt% Sc<sub>2</sub>O<sub>3</sub>) lie along a well-defined line (we also include one Ti-, Sc-rich

burnettite analysis in this grouping). The davisites in this grouping can be as Sc-rich as those observed by El Goresy et al. (2002) in CTA Efremovka 101.1, but they also have considerably more V (7–8 wt% V<sub>2</sub>O<sub>3</sub> versus 1–2 wt%). Mass balance calculations show that data in the high Sc-portions of this grouping are generally consistent with two endmembers; one is paqueite and the other is a mixture of the ultrarefractory minerals eringaite and warkite. This is discussed below after introducing mass balance calculations involving paqueite. Observed low-Sc, high-Ti grossmanites (<2 wt% Sc<sub>2</sub>O<sub>3</sub>) range from 13 to 23 wt% TiO<sub>2</sub>\* (total Ti), generally showing decreasing V with increasing Ti\*.

Most burnettites (and kushiroites) in *CGft-12* plot near the origin in Fig. 8a (i.e., they are Sc-, Ti-poor). Two burnettites are, however, relatively Ti-rich. One of these plots with the Sc-rich grossmanites and is essentially a grossmanite with just enough V to qualify as a burnettite. The other plots between the bulk of burnettites plotting near the origin in Fig. 8a and the low-Ti end of the low-Sc grossmanites. Mass balance calculations (and other panels in Fig. 8) suggest that this analysis shows an affinity for the grossmanites and not the main group of low-Ti, low-Sc burnettites. We, therefore, include these burnettites in the Sc-, Ti-rich group and show below that the mechanism of formation is the same for all of these clinopyroxenes. Finally, with regard to Fig. 8a, we note that the clinopyroxenes in A-WP1 are most closely related compositionally to the davisite–grossmanite grouping in Fig. 8a and we discuss them together below.

The theme of grossmanites and davisites in *CGft-12* all being related can also be elicited from Fig. 8b. Based on Mg–Ti\*, clinopyroxenes from A-WP1 are, again, closest in composition to this grouping. In Fig. 8c, davisite–grossmanites in *CGft-12* show an overall negative correlation in Ti\*–V, although the low-Sc grossmanites have a positive correlation. The negative correlations for davisite + Sc-rich grossmanite in Sc–Ti–V (Figs. 8a–c) are important in deciphering the significance of crystallization from a melt in determining the compositions of clinopyroxene because positive correlations would be expected in that case (e.g., Simon et al., 1999). The Sc-rich clinopyroxenes (Fig. 8a) probably did not crystallize from a late-stage melt of bulk CAI and, to the extent paqueite is implicated in their formation, it also did not crystallize from a bulk melt. It is, however, possible that V-rich condensate phases melted during a thermal event, creating a V-rich local melt that did not homogenize before being swallowed by the advancing crystallization front of the host melilite. In such a scenario, chemical signatures of the original condensate grains would have been largely retained in the crystallized grains. The irregular and



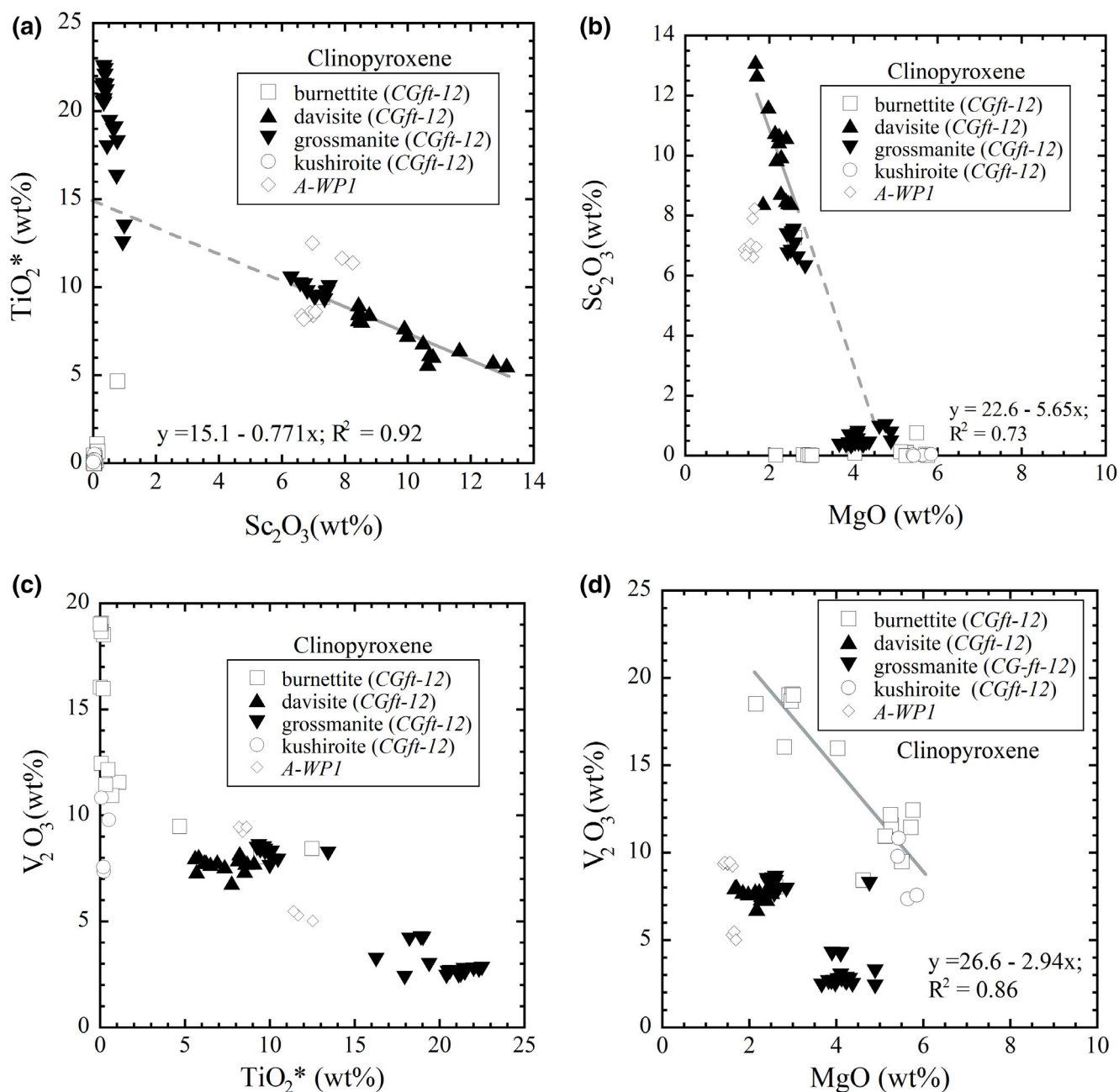


Fig. 8. Composition (wt% oxides) of clinopyroxene in *CGft-12* and *A-WP1*. Clinopyroxenes in *CGft-12* are coded according to mineral name. Mineral names for clinopyroxenes in *A-WP1* (burnettite, davisite, grossmanite) are not distinguished. a)  $\text{Sc}_2\text{O}_3$ - $\text{TiO}_2^*$  (all Ti calculated as  $\text{TiO}_2$ ). An unweighted linear regression through the Sc-rich points ( $\text{Sc}_2\text{O}_3 > 6$  wt%) is shown in the panel for *CGft-12*. b)  $\text{MgO}$ - $\text{Sc}_2\text{O}_3$ . An unweighted linear regression for  $\text{Sc}_2\text{O}_3 > 6$  wt% is shown. c)  $\text{TiO}_2^*$ - $\text{V}_2\text{O}_3$ . d)  $\text{MgO}$ - $\text{V}_2\text{O}_3$ . An unweighted regression through burnettites and kushiroites is shown (excluding the Ti-rich burnettite that plots with davisite-grossmanites in panels a and b). (Color figure can be viewed at [wileyonlinelibrary.com](http://wileyonlinelibrary.com).)

rounded shapes of many clinopyroxene grains are consistent with partial dissolution and may hint at more than one heating event or the survival of original condensate crystals or relict igneous grains from a previous melting event. Relict clinopyroxene is sometimes invoked to explain the presence of

clinopyroxene blebs in the mantles of type B1 inclusions (e.g., Simon et al., 1991). Clinopyroxene compositions from *A-WP1* invariably plot near those of davisites from *CGft-12*, consistent with a similar origin.

The second grouping of clinopyroxenes (kushiroites and most burnettites) is dominated by variations in V.

These grains appear not to be mixtures. Hypothetical endmember compositions (e.g., by extrapolation of composition trends) are not plausible candidates for being at the low-Ti end of the mixing line for the davisite–grossmanite grouping as they are too low in Ti and too high in Mg at any given V content (e.g., Figs. 8a and 8d). We also note, via Fig. 8d, that concentrations of Mg and V in clinopyroxenes from the burnettite–kushiroite grouping in *CGft-12* are negatively correlated but that Sc-Ti\* values are positively correlated.

Overall, the compositions of clinopyroxenes in A-WP1 and *CGft-12* suggest that there are two main populations, even though both groups are anomalous in being V-rich relative to most observed clinopyroxenes in type A or ultrarefractory inclusions. The positive Sc-Ti\* correlation for the kushiroite–burnettite grouping is potentially consistent with crystallization from a melt where both elements are compatible, but the negative correlation for the davisite–grossmanite is inconsistent with crystallization from a melt. Finally, we note that clinopyroxene included in melilite from A-WP1 and *CGft-12* usually consists of isolated grains (e.g., Fig. 3b). We also observed two examples of paqueite coexisting with clinopyroxene. If these grains equilibrated with each other, they can be used to get a rough idea of partitioning between the two phases. The example shown in Fig. 2c leads to apparent partition coefficients,  $D_i^{Gsm/Paq}$  of 36 for Mg, 5 for Sc, 2 for V, 1 for Zr, and 0.5 for Ti\*.

### Other Phases

In general, the primary phase assemblage of a type A inclusion, whether fluffy or compact, consists of coarse grains of melilite with inclusions in various amounts of spinel, hibonite, perovskite, alloys, and clinopyroxene, usually grossmanite and/or davisite (e.g., MacPherson & Grossman, 1984; Simon et al., 1999), and occasionally of interstitial phases. A-WP1 and *CGft-12* contain each of these phases plus paqueite and the clinopyroxene burnettite. A-WP1 also contains beckettite and a grain of baghdadite (Ma, 2018). Phase assemblages in *ALH1* and *TS-28* are consistent with this motif, except that clinopyroxene was not observed in *TS-28* and neither inclusion contains paqueite.

FTAs in CV3 chondrites are invariably altered to fine-grained assemblages of grossularite, anorthite ± nepheline after melilite plus a variety of phases altered from primary inclusions in the melilite. Neither of the new minerals discussed here formed through this alteration/metamorphic process. In this section, we give brief descriptions of the primary phases included in melilite other than the new minerals. It should be kept

in mind that, where isolated, these phases are not necessarily cogenetic, with each other or, for that matter, with the host melilite. The reservoir of grains that the melilite incorporated may well have contained material from more than one source and they may have formed in environments not directly related to their melilite host. Indeed, we conclude that at least two distinct environments were sampled by *CGft-12*.

### Spinel

Spinel is the most prominent inclusion in melilite from A-WP1 and *CGft-12*. The grains are euhedral to subhedral (Figs. 1 and 2a) with compositions generally close to the (Mg,Fe)Al<sub>2</sub>O<sub>4</sub> binary. The Fe is thought to have been introduced into Allende CAIs during a secondary metasomatic event (Kurat et al., 1975; Paque et al., 2007). The origin of minor V in the spinel is less certain. Connolly and Burnett (1999) and Connolly et al. (2003) explored V concentrations in spinel from type B1 inclusions and concluded that the V largely reflected reequilibration with melt. Paque et al. (2007) observed examples of highly localized enrichments of V in spinel associated with the release of correlated V-Fe from oxidizing alloys and adjacent phases during planetary metamorphism in an Allende type B1 inclusion but, typically, V and Fe were uncorrelated. Figure 9 shows cations of V pfu in spinels from type A inclusions included in melilite or alteration products as a function of Fe. In *CGft-12*, Fe contents are quite variable (0.02–0.26 cations pfu for data from eight crystals), but V is consistently ~0.03 cations (spinel in the rim has much lower V, ~0.005 cations pfu). There is no correlation of V content with Fe or with grain position within the inclusion and the most likely explanation is that the V reflects a primary, pre-alteration signature. *CGft-12* captured a population of spinels with ~0.03 cations pfu of V. Maximum V concentrations in spinel from type B1 inclusions are comparable (i.e., 0.02–0.03 cations pfu; e.g., Connolly & Burnett, 1999), although most spinels appear to have been modified by reequilibration with a melt. The Fe-V pattern for spinel in A-WP1 is fundamentally different. Here, V concentrations at low Fe contents are comparable to those observed in *CGft-12* (i.e., ~0.03 cations pfu), but V generally increases with increasing Fe and, in particular, the highest V concentrations are observed in the most hercynitic spinels. The connection between Fe concentrations and V enhancements above 0.03 cations pfu suggests that V was mobile in A-WP1 during the Fe-metasomatism event. The source of the V must have been internal to the inclusion prior to alteration (i.e., not from host Allende matrix, as otherwise such enhancements would be endemic among Allende type A inclusions).



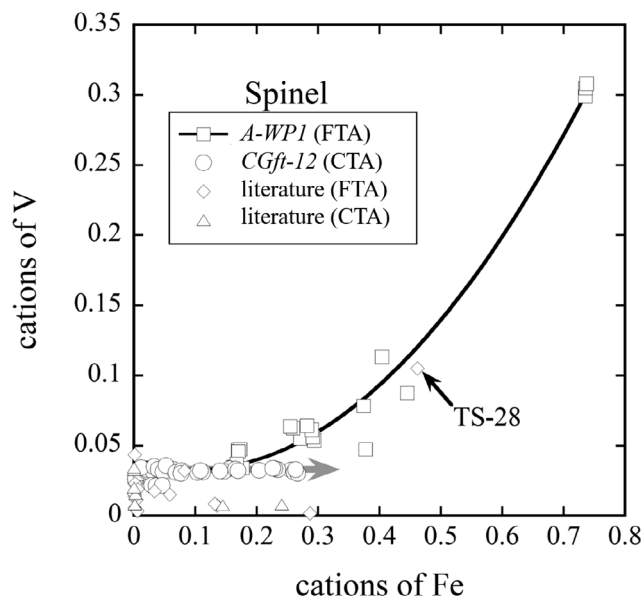


Fig. 9. Cations of Fe versus V in FTAs. The curve represents an unweighted second-order polynomial regression through data for A-WP1 from this study. The gray line with an arrowhead is drawn through the average V content for data from *CGft-12*. Literature data are taken from Allen et al. (1978), Fahey et al. (1987), Grossman (1975), Kawasaki et al. (2017), Krot et al. (2019), Lin and Kimura (2003), MacPherson and Grossman (1984), and Srinivasan et al. (2000).

Data from the literature are too sparse to address the details of V evolution as seen through spinel in FTAs, but typically no correlation is observed between V and Fe (MacPherson & Grossman, 1984; Simon et al., 2001). Only one analysis, from TS-28 (MacPherson & Grossman, 1984), is consistent in Fig. 9 with the Fe-rich data from A-WP1 and could reflect V enrichment during Fe-metasomatism. The others display no evidence for secondary V enrichment. Indeed, there appears to be an anticorrelation between V and Fe for Fe-enriched spinels described in the literature (Fig. 9). Overall, spinel in most type As has variable V concentrations  $\leq \sim 0.04$  cations pfu that are likely primary with an occasional inclusion showing significant mobility of V during Fe-metasomatism. The source of V for these rare occurrences (A-WP1, possibly TS-28) is unknown but could be related to the alteration of V-rich phases including, as suggested by Paque et al. (2007), to oxidation of nearby alloys or to the reaction of V-rich magnetites derived from such alloys. For both *CGft-12* and A-WP1, spinel inclusions contained a primary  $V_2O_3$  content of  $\sim 0.04$  wt%. Only one source appears to have been sampled in contrast to the bimodal distribution of V concentrations observed for paqueite and perovskite.

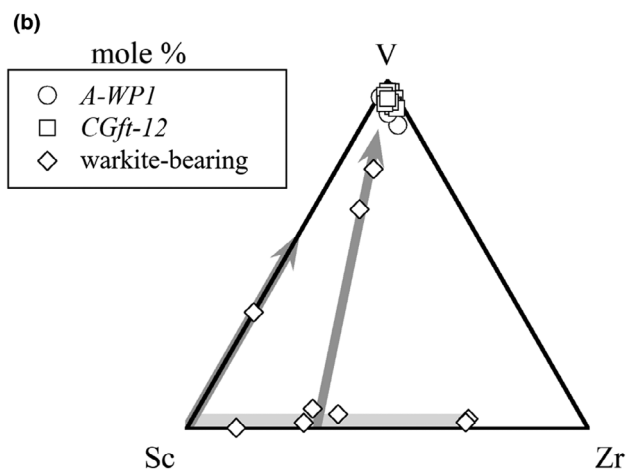
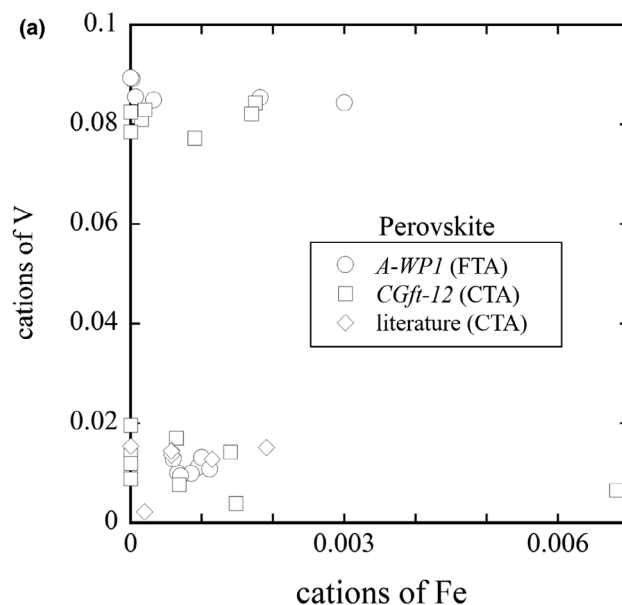


Fig. 10. Compositions of perovskite. a) Cations of V as a function of Fe in A-WP1 and *CGft-12*. Literature data from Srinivasan et al. (2000) and El Goresy et al. (2002). b) Cations of Sc, V, and Zr in perovskite from the type A inclusions A-WP1 and *CGft-12* and from warkite-bearing inclusions (Ma et al., 2020).

#### Perovskite

Perovskite occurs decorating spinel and as rare isolated grains included in the melilite of A-WP1 and *CGft-12* (Figs. 1c and 3b; see also figs. 1 and 2 in Simon et al., 1999). The compositions are all close to nominal  $CaTiO_3$  but with up to 5 wt%  $V_2O_3$  ( $\sim 9$  mole %). From Fig. 10, V concentrations for perovskite in both inclusions cluster around either 0.01 or 0.08 cations pfu with no correlation between V and Fe and we observed no connection between the chemistry of a perovskite grain and its shape or style of occurrence.

We interpret these results to imply (1) that the observed V in these FTA perovskites predates the Fe-metasomatism event and (2) melilite in *CGft-12* and A-WP1 captured perovskite from at least two distinct regimes, one of which could involve small-scale partial melting. The bimodal distribution of V in both paqueite and perovskite is consistent with grains of these two phases being drawn from the same reservoirs. Based on mass balance calculations discussed above, variations in the compositions of clinopyroxene inclusions in *CGft-12* did not involve perovskite. Yet, they too appear to have been drawn from two main lineages.

Direct comparisons of chemistry for perovskite in A-WP1 and *CGft-12* with those from other type As are not possible at present as none of the available analyses of perovskite from type As in the literature included V (e.g., Allen et al., 1978; Grossman, 1975). However, analytical sums for most of these analyses were close enough to 100 wt% and the formulas to stoichiometric  $\text{CaTiO}_3$  to at least suggest that V contents of these grains were lower than the several wt% observed in some perovskites from A-WP1 and *CGft-12*. More complete analyses are available for perovskite from ultrarefractory inclusions containing warkite (Ma et al., 2020). Perovskites from the type A inclusions plot near the V-vertex in Fig. 10b. Most of the perovskites from warkite-bearing inclusions are far lower in V, although inclusions *Moss-1* and *V13* are exceptions. Given the broad-spectrum of Sc/Zr ratios in perovskite from the warkite-bearing inclusions and V enrichment in some of them, it is possible that the perovskites in A-WP1 were derived from a population of perovskites similar to those observed in warkite-bearing inclusions through enrichment in V and  $\text{CaTiO}_3$  (thereby diluting Sc and Zr). The observed enrichments in V could reflect a widespread event that affected pre-existing perovskites in a process that was more efficient than reactions leading to the destruction of perovskite. Perovskite, for example, does not appear to have been a significant direct source of Ca or Ti in the observed clinopyroxenes. Vanadium enrichment may have been a key indicator process marking the contribution of material from an ultrarefractory environment.

### Hibonite

Hibonite grains in A-WP1 and *CGft-12* have highly variable chemistry, in contrast to bimodal (paqueite, clinopyroxene, perovskite) or singular (spinel) populations based on V. Concentrations of Ti in A-WP1 and *CGft-12* hibonites (1.4–9.6 wt%  $\text{TiO}_2$ ) and Mg (1.0–4.0 wt%  $\text{MgO}$ ) are quite variable and correlated, which is typical of hibonites in type A inclusions (1.2–8.3 and 0.5–4.3 wt%, respectively; Allen et al., 1978; Bischoff

et al., 1993; Grossman, 1975; Lin & Kimura, 2003; Lin et al., 2003; MacPherson & Grossman, 1984; Paque, 1987; Simon et al., 2001; Weber & Bischoff, 1997). This reflects a charge-coupled substitution for Al,  $2\text{Al}^{3+} = \text{Mg}^{2+} + \text{Ti}^{4+}$  (e.g., Allen et al., 1978; Simon et al., 2001). However, hibonites in A-WP1 and *CGft-12* also have rather variable concentrations of  $\text{V}_2\text{O}_3$  (0.0–2.2 wt%) and FeO (0.0–0.7 wt%), which again is comparable to ranges reported in type A inclusions (0.02–1.6 and 0.0–0.7 wt%, respectively), with the exception (3.6 wt% FeO) of a highly altered grain of hibonite-(Fe) (now renamed chihuahuaite) described by Ma (2010). We did not observe correlations between Fe and V concentrations, although V contents for hibonite from *CGft-12* do tend to decrease with increasing Fe (i.e., hibonite may actually lose V during Fe-metasomatism). It is worth noting that a continuum of V contents in hibonite is a different pattern than observed for paqueite and perovskite, where V concentrations were bimodal and highly restricted. Given the broad range in Mg-Ti and V, hibonite in type As accessed a broad range of environments (i.e., the population of hibonites was well mixed but not homogenized) and that the process(es) leading to a bimodal distribution of V contents for paqueite and perovskite did not occur for hibonite. Moreover, we see no evidence in the clinopyroxene compositions for a significant contribution from hibonite.

### Alloys

Alloys in A-WP1 are small (<650 nm) but enriched in refractory metals. Compositions are shown in Fig. 11

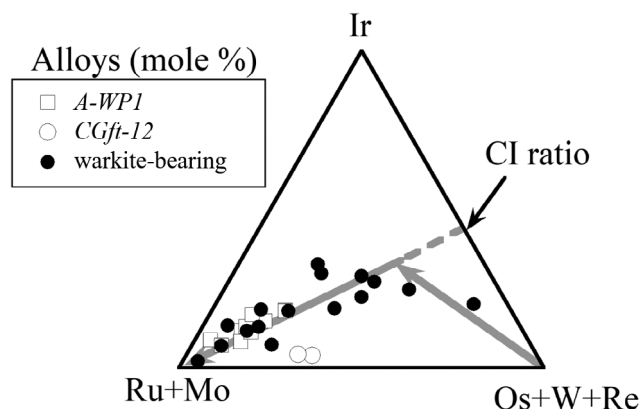


Fig. 11. Alloy compositions in A-WP1 and *CGft-12* expressed in terms of Os+W+Re, Ir, and Ru+Mo with mole% Fe + Ni < 40% and Pt < 5%. Data for A-WP1 are taken from Paque (1989) and this study and those for *CGft-12* are from this study. Those for warkite-bearing inclusions are from Ma et al. (2020). The CI ratio for Ir/(Os+W+Re) is indicated. Gray arrows indicate the direction of equilibrium alloy compositions as a function of increasing degree of condensation in a cooling gas of solar composition.

for *CGft-12* and A-WP1, organized in terms of the highly refractory elements W + Os + Re, the slightly less refractory Ir, and the moderately refractory Mo + Ru (i.e., it ignores the least refractory elements present in the alloy, such as Pt, Ni, and Fe). Also shown is the trajectory for alloy compositions during equilibrium condensation from a cooling gas of solar composition from Campbell et al. (2001). This diagram was used by Ma et al. (2014b, 2020) to show variations in chemistry for alloys from ultrarefractory inclusions. Data for warkite-bearing inclusions (Ma et al., 2020) are shown for reference. From Fig. 11, the alloys in A-WP1 are decidedly less refractory than many of the alloy grains in warkite-bearing inclusions but nevertheless consistent with expectations for equilibrium condensation. The melilite host in A-WP1 accessed a generally more evolved collection of metal than did warkite-bearing inclusions, missing the more Os-, W-enriched alloys found in the latter. Alloys in *CGft-12* include Ni-, Fe-rich metal ( $\text{Ni}_{0.68}\text{Fe}_{0.30}\text{Co}_{0.02}$ ;  $\text{Ni}_{0.67}\text{Fe}_{0.32}\text{Pt}_{0.01}$ ;  $\text{Ni}_{0.87}\text{Fe}_{0.12}\text{Co}_{0.01}$ ;  $\text{Ni}_{0.49}\text{Fe}_{0.36}\text{Pt}_{0.10}\text{Rh}_{0.03}\text{Mo}_{0.02}$ ) and small (<600 nm) refractory grains ( $\text{Ru}_{0.48}\text{Os}_{0.27}\text{Fe}_{0.18}\text{Ir}_{0.03}\text{Ni}_{0.02}$ ;  $\text{Ru}_{0.47}\text{Os}_{0.22}\text{Fe}_{0.17}\text{Ir}_{0.03}$ ). In Fig. 11, the refractory grains from *CGft-12* plot at much lower Ir contents than expected for equilibrium condensates. These grains could reflect an unusual environment of formation but, more likely, constitute either mixtures of Os-W- and Ru-Mo-enriched alloys within the activation volume for the analyses or of homogeneous alloys derived from such mixtures through a thermal event.

## DISCUSSION

A basic issue for the origin and evolution of type As in general and CTAs in particular is the extent to which melting was involved in producing the observed minerals and their chemistries. FTAs are generally thought to be direct gas–solid condensates (e.g., MacPherson & Grossman, 1984). As noted above, melilite in most, if not all, CTAs is likely to have been crystallized from a melt or derived from material that had been melted at some point with volatilization because common enrichments in the heavy isotopes of Mg and Si (Aléon et al., 2018; Clayton et al., 1988; Grossman et al., 2008; Mendybaev et al., 2017) are otherwise hard to explain. These CAIs were, however, subjected to one or more subsequent thermal events and it is the nature of these events and implications for existing minor phases, including the new minerals burnettite and paqueite, that concern us here. Whether the most recent thermal event(s) led to significant melting or metamorphic recrystallization of melilite is a key focus for many studies of CTAs. Simon et al. (1999) summarized observations indicating that a CTA

melted at least partially to produce the observed inclusion. These include the rounded form of the inclusion, axiolytic growth texture of melilite crystals from rim inward, igneous partitioning of REEs, positive correlation of V and Sc in clinopyroxene (both elements are compatible in clinopyroxene), which should lead to correlated enrichments during crystallization from a melt (provided clinopyroxene was the only V-, Sc-rich phase in the instantaneously crystallizing phase assemblages), occurrence of clinopyroxene and perovskite in interstices between melilite crystals, and the presence of perovskite–clinopyroxene–spinel symplectites. Variations in oxygen isotopic compositions have also been proposed to indicate a melting event (e.g., Aléon et al., 2007; Suzumura et al., 2021). Metamorphic signatures include homogenous melilite compositions, straight melilite–melilite grain boundaries, and 120° triple junctions for melilite. *CGft-12* is rounded and melilite is variably zoned (Ak13–Ak45), consistent with some melting. However, interstitial symplectites were not observed and Sc and V in davisite–grossmanites are negatively, not positively, correlated (Fig. 8a), implying that the chemistry for these clinopyroxene inclusions in melilite predated melting in post-evaporative events. The inclusions in melilite from *CGft-12* and A-WP1 were derived at least in part from environments anterior to the current inclusion.

## Origin of Paqueite—Condensation and Exsolution

Paque et al. (1994) produced paqueite during late-stage dynamic crystallization of a type B1 bulk composition, but these authors also noted a predilection for meteoritic paqueite to occur at the intersection of cleavage planes within melilite, which would not be expected for igneous inclusions. Paqueite is invariably an inclusion within melilite in coarse-grained CAIs and not interstitial between grains as would be expected for a late-crystallizing igneous phase. Meteoritic paqueites described in this work and the literature probably did not crystallize from a late-stage melt, although this does not mean that at least some of the observed crystals of paqueite did not crystallize from a melt. Paqueite coexisting with grossmanite could, in principle, have crystallized from a melt, although even for the grain in Fig. 2c, the irregular shape of the enveloping clinopyroxene is superficially inconsistent with this possibility.

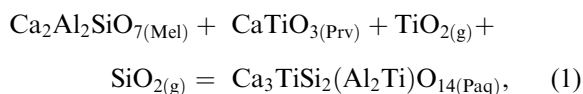
As noted above, apparent partition coefficients between coexisting paqueite and grossmanite show that V and Sc are much more compatible in the clinopyroxene, so that co-crystallization of paqueite and clinopyroxene would not destroy a V-Sc correlation,



assuming the mode of instantaneously crystallizing paqueite during clinopyroxene crystallization was not much greater than that of the clinopyroxene.

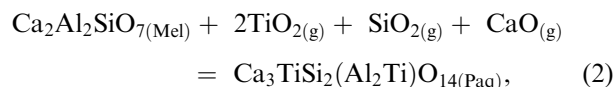
The exsolution of paqueite from nonstoichiometric melilite needs to be considered. Prismatic inclusions with long axes tending to align with or be perpendicular to cleavage cracks within the melilite are Sc- and V-poor (Fig. 6b). These grains are potential candidates for exsolution, although it is also possible that the correlation with cleavage was promoted by paqueite inclusions initiating the cleavage, as is often observed for inclusions in steel (e.g., Fairchild et al., 2000). The paqueites from *CGft-12* are relatively low in Sc (0.12–0.22 wt% Sc<sub>2</sub>O<sub>3</sub>) but mostly high in V (2.9–4.4 wt% V<sub>2</sub>O<sub>3</sub>) and, of course, extremely high in Ti. If they were exsolution products, we would expect relatively low Sc, as Sc is highly incompatible in the putative source melilite (e.g., Beckett et al., 1990), but V and Ti contents of potential source melilite are also quite low. Even dendritic melilite has essentially stoichiometric compositions (Stolper & Paque, 1986), which weighs against the idea that exsolution of paqueite attended the relaxation of a nonstoichiometric melilite back to a stoichiometric form. An alternative is that paqueite grows epitaxially on melilite within small melt inclusions or as condensates on melilite. However, these grains are not accompanied by co-crystallizing phases, which might be expected at least occasionally in such melt pockets. Many paqueite grains in *CGft-12* are similar to those in A-WP1, but some are quite different. These are often rounded/etched, larger, and frequently associated with grossmanite (Figs. 2b and 2c). In one example (Fig. 2c), paqueite is completely enclosed in grossmanite. These grains are not good candidates for exsolution products.

A third potential mode of formation for paqueite in type A inclusions is condensation from a vapor, which, on balance, we favor for most occurrences, although possibly with later modification. The occasional occurrence of paqueite with clinopyroxene suggests that grossmanite followed or was coeval with paqueite. We also note that paqueite and perovskite (also hibonite and spinel) are not texturally associated. This observation likely means that reactions such as



where “Mel” refers to melilite, “Prv” to perovskite, “g” to vapor, and “Paq” to paqueite were not significant causes of paqueite formation. As an aside, we note that, in the above reaction, TiO<sub>2</sub> and SiO<sub>2</sub> are arbitrary species, although they constitute a thermodynamically

valid representation. If the reaction were to take place in a cooling gas of solar composition, SiO(g) would be the dominant species for Si in the vapor and TiO(g) or TiO<sub>2(g)</sub> for Ti (e.g., Sharp & Huebner, 1990). Any such dominant species are thermodynamically connected to the ones used in Equation 1 and desired species could be substituted with the reaction being appropriately balanced using oxygen. Moreover, one could construct similar representations for equilibration with a melt (i.e., replace “[g]” in Equation 1 with “[liq],” where “liq” refers to compounds in the melt). We suggest that a more appropriate reaction describing the formation of paqueite is



Like reaction (1), reaction (2) requires that melilite be condensed before paqueite (i.e., gehlenite is a reactant) and that Ti be incompletely condensed, but it does not require perovskite to participate in the paqueite formation reaction. Indeed, due to structural similarities, once gehlenite condenses, melilite provides a highly suitable substrate for the nucleation and epitaxial growth of paqueite. It also provides an abundance of Ca and Al needed to construct the phase. Assuming the vapor pressure of Ti was not limiting, one might therefore expect paqueite to be far more common than it is. The source of paqueite’s rarity likely lies in the relative stabilities of paqueite and clinopyroxene. Paqueite may have a stability field in nebular environments and, in the presence of melilite, it has a ready nucleation site, but once clinopyroxene becomes stable, any exposed paqueite becomes highly reactive. We see two possibilities for the survival of a condensate paqueite grain in a CTA. The possibilities are that the (1) pre-existing grains of paqueite are present in the proto-inclusion and survive at the peak temperature for the bulk CAI (i.e., the peak temperature for the CTA is below the liquidus for paqueite and the dissolution rate of paqueite into the CTA melt is too slow to destroy the grain) or (2) the paqueite was introduced to a molten or partially molten droplet during cooling under conditions in which the grain survived long enough to be incorporated into melilite (i.e., there was a late-refractory dust addition to the molten or partially molten droplet). The grain was never exposed to the peak temperature for the inclusion.

### Crystallization of Paqueite from Melt

Analyses of clinopyroxene (e.g., Fig. 12) are consistent with paqueite being a reactant in the formation

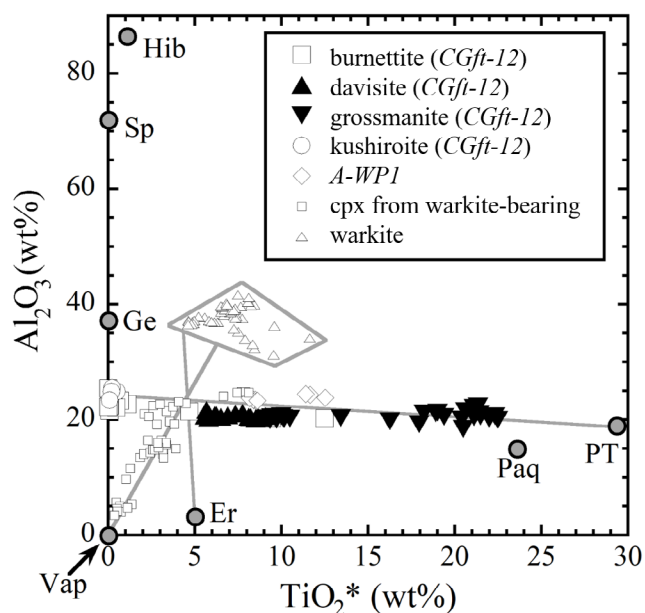


Fig. 12.  $\text{TiO}_2^*$ - $\text{Al}_2\text{O}_3$  for clinopyroxenes in *CGft-12* and A-WP1 (this study) and warkite-bearing inclusions (Ma et al., 2020). Also shown are compositions of other phases. Er = eringaite (Ma et al., 2020); Ge = endmember gehlenite; Hib = hibonite (this study); Paq = paqueite in *CGft-12*; PT = Ti-endmember of paqueite,  $\text{Ca}_3\text{TiSi}_2(\text{Al}_2\text{Ti})\text{O}_{14}$ ; Sp = endmember spinel; Vap = vapor. Note that the plotted composition of the vapor assumes that partial pressures of Ti and Al species in the vapor are negligible.

of V-, Sc-rich clinopyroxenes. In the above section, we evaluated expectations for the formation of paqueite as a condensate but noted that the original condensate grains could have been lost to a melting event. Here, there are two basic possibilities. First, there may be inclusions of condensate grains incorporated into melilite that melt and recrystallize during a subsequent heating event, or act as nucleation points for clinopyroxene. The grossmanite–paqueite pairs shown in Fig. 2c are examples. A second possibility is that perovskite partially dissolved into melt and that the Ti, so freed, was utilized by crystallizing paqueite and clinopyroxene. A direct reaction between perovskite and melt to form these phases is, however, contraindicated because perovskite grains in *CGft-12* do not show rimming clinopyroxene or paqueite and neither clinopyroxene nor paqueite contains residual perovskite. Both condensate and crystallization motifs are possible. It is perhaps worth noting that there are low and high V families of paqueite. We argued above that low-V paqueite is a likely reactant for the formation of high Sc-, Ti clinopyroxene and that ultrarefractory phases are also implicated. Perovskite is inconsistent with this derivation.

### Origin of Burnettite and Other Clinopyroxenes

Burnettite is a new refractory mineral. It is Sc-rich (coexisting melilite is Sc-, V-poor, <0.03 wt%), joining other Sc-rich refractory minerals from carbonaceous chondrites including allendeite, tazheranite, davisite, kangite, panguite, eringaite, and thortveitite. Burnettite is also extraordinarily V-rich. In CAIs, only the primary V-rich diopsides described by Armstrong et al. (1985) have comparable  $\text{V}_2\text{O}_3$  contents. Yttrium and the REE were not detected in the clinopyroxenes of A-WP1 and *CGft-12* by EPMA, but the high Sc in clinopyroxenes of the grossmanite–davisite grouping, which includes some burnettite, is consistent with derivation from an ultrarefractory parent and the high  $\text{Ti}^{3+}/\text{Ti}^{4+}$  suggests reducing conditions. Coexisting paqueite (Figs. 2b and 2c) is Sc-poor, but, based on stoichiometry, it also likely contains significant concentrations of  $\text{Ti}^{3+}$ .

The chemistry of  $\text{R}^{3+}$ -enriched clinopyroxenes in *CGft-12* and A-WP1 constrains the origin because it limits possible formation reactions. Compositions of the Sc-, Ti-enriched clinopyroxenes in *CGft-12* can be mass balanced using paqueite, one or both of the ultrarefractory phases eringaite and warkite, and gehlenite with gaseous contributions for Si and V. There are two distinct groups of clinopyroxenes in type A inclusions. Figure 12 shows  $\text{TiO}_2^*$ - $\text{Al}_2\text{O}_3$  for clinopyroxenes from type A inclusions obtained in this study and warkite-bearing inclusions from Ma et al. (2020). Ti-Al relationships among Ti-enriched clinopyroxenes (davisites, grossmanites, and some Ti-rich burnettites) from *CGft-12* and A-WP1 are consistent with sourcing from paqueite, melilite, and one or more of eringaite, warkite, and vapor. Note that endmember paqueite is a better fit as the Ti-rich contributor to clinopyroxene than is the observed V-rich paqueite. This suggests that it was low-V paqueites that were the parents for high-Ti clinopyroxenes. The Ti-rich clinopyroxenes also generally have high Sc contents, which most likely comes, based on mass balance using numerous candidate ultrarefractory phases, from eringaite and warkite. Note also that the low-Ti limit for davisite–grossmanite in Fig. 12 is consistent with the exhaustion of one or more of paqueite, eringaite, and warkite. Although a few of the clinopyroxenes from warkite-bearing inclusions have compositions consistent with the Ti-rich group from *CGft-12*, most of them are off-trend relative to the high-Ti group and consistent with warkite as a major contributor to the Ti, as noted by Ma et al. (2020). Kushiroites and most burnettites in *CGft-12* are high in V and low in Sc and Ti. From mass balance and a condensation perspective, these grains likely formed from gehlenite and vapor (source of V and Si) with minor contributions from a low-Ca,

aluminous phase (e.g., spinel). Paqueite was not involved. Beckettite, a vanadium calcium aluminate, was also not a significant reactant. It is also notable that no combination of paqueite and clinopyroxene compositions observed in *CGft-12* can account for the bulk composition of the observed perovskite. This would have been expected had perovskite been the sole source for these elements. Therefore, perovskite was not a reactant in the formation of clinopyroxene in *CGft-12*. Precursors to perovskite and clinopyroxene in *CGft-12* formed and arrived separately.

Results of the above mass balance calculations are consistent with an origin for the observed clinopyroxenes via combinations of various condensate grains (i.e., their compositions reflect condensate precursors). It does not, however, follow that the observed grains must therefore be condensates. Available phase equilibria provide two key constraints. At temperatures near or above the liquidus for the bulk inclusion, any crystal within a precursor inclusion would be exposed to the melt and, given sufficient time, it would dissolve. For CTA inclusions, liquidus temperatures are roughly 1450–1550 °C, with temperature increasing with increasing mode of spinel and/or decreasing average Ak for the melilite (Paque & Stolper, 1984; Stolper, 1982). To account for observed bulk compositions and isotopic fractionations, at least one brief excursion to temperatures near or above the liquidus was likely in the history of some CTAs (e.g., Mendybaev et al., 2021). A condensate grain whose liquidus temperature was below that of the surrounding melt would itself melt and therefore be destroyed, although the chemical and isotopic signatures could be retained if the thermal event was too brief to allow the homogenization of the anomalous melt produced by the condensate crystal or if the condensate crystal was introduced in a late salting event during cooling, as is sometimes proposed to account for nucleation in chondrules (e.g., Connolly & Hewins, 1995). A second important temperature is the solidus for the melilite hosting an inclusion. For clinopyroxene and paqueite inclusions in *CGft-12*, host melilite is typically ~Ak30, whose solidus is ~1425 °C (Mendybaev et al., 2006). Once enclosed in the host melilite, an inclusion may melt, recrystallize, or react with the melilite, but it will survive as an inclusion as long as the host melilite survives. In principle, one could directly constrain the thermal history of the host inclusion through a knowledge of the stabilities of the inclusion phases and their phase equilibria in melilite-saturated environments. Diopside, which is a significant component in the clinopyroxenes (0.1–0.3 pfu; cf. Table 2), melts at 1392 °C (Adams, 1914; Hudon et al., 2005). An endmember diopside grain would immediately melt if

exposed to a temperature higher than 1392 °C, so a surviving condensate diopside grain in melilite of a CTA would require introduction at a lower temperature (i.e., a late salting event). Unfortunately, the effects of burnettite, davisite, grossmanite, and  $\text{CaTi}^{4+}\text{Al}^2\text{O}_6$  components, which constitute 70–90% of the clinopyroxene compositions in *CGft-12*, on the liquidus temperature are unknown, as are the liquidus temperatures for meteoritic paqueite. It seems unlikely, however, that their liquidus temperatures are so high that the observed clinopyroxenes could have survived the high peak temperatures invoked for evaporative processes that affected the bulk CAIs (e.g., Mendybaev et al., 2021). Nor are there phase diagrams that describe the stabilities of these phases in melilite-bearing systems or in bulk CTA-like melts. Predicting responses of observed clinopyroxene or paqueite inclusions in *CGft-12* or A-WP1 for a specific thermal history could introduce some powerful constraints, but it is not currently possible to access this information.

### Significance of Vanadium in CAI Phases

Vanadium is a moderately refractory element in nebular settings. If solution into low-V phases is suppressed,  $\text{V}_2\text{O}_3$  and VO are the first V-rich phases to condense at equilibrium, 1429 K in a cooling gas of solar composition referenced to a total pressure of  $10^{-4}$  atm (Lodders, 2003). This is substantially lower than for the ultrarefractory elements like Zr ( $\text{ZrO}_2$ ; 1764 K) and Sc ( $\text{Sc}_2\text{O}_3$ ; 1659 K) and of refractory phases such as hibonite (1659 K), perovskite (1593 K), grossite (1542 K), and melilite (gehlenite at 1529 K) but higher than spinel (1397 K), anorthite (1387 K), or forsterite (1354 K), where all of the stated condensation temperatures are taken from Lodders (2003). That said, it is clear from data in this and other studies (e.g., Simon et al., 1999; Paque et al., 2007; Ma et al., 2020) that V is soluble at relatively high concentrations (>~1 wt%) in clinopyroxene, spinel, hibonite, paqueite, rhönite, warkite, eringaite, and perovskite. Since the solar abundance of V is only 0.5% of Al + Ti on a weight basis, all of the V could, in principle, be accommodated during condensation as a minor element in refractory and ultrarefractory oxide phases. Condensation calculations (e.g., Lodders, 2003) predict that  $\text{V}_2\text{O}_3$  and VO are the condensate sinks for V, but these phases are not observed in meteorites and probably never become stable in a cooling gas of solar composition due to the presence of other phases taking up minor amounts of V. There are no thermodynamic data for the solution of V into most of these phases, making this V solubility phenomenon invisible to most condensation calculations. This is a recognized limiting



problem for using V-bearing phases to constrain nebular environments. Lodders (2002), for example, did some exploratory calculations for condensation in the atmospheres of dwarf stars that considered the ideal solution of vanadium oxides into other phases. Such calculations are, however, hampered by the absence of any underpinning thermodynamic data.

The presence of V-enriched phases, clinopyroxene, perovskite, and paqueite in A-WP1 and *CGft-12* is consistent with the acquisition of a collection of grains sampling a region in which V was tracing evolution. Melilite, which was critical to the formation of paqueite and clinopyroxene, has a low solubility for V, but most of the phases observed as inclusions in host melilite can take in significant concentrations of this element and we can, therefore, use this feature to constrain their formation. A basic condensation scenario for phases included in melilite from type A inclusions that derives in part from the observed V would be:

(1) *Condensation of low-V warkite, eringaite, hibonite, perovskite, and spinel.* Other refractory and ultrarefractory phases, such as tazheranite, allendeite, corundum, grossite, etc., would presumably also have appeared by the time/place according to the above listed minerals, but they are not included in the phases observed or inferred to have been present in type As.

(2) *Condensation of gehlenite.*

(3) *Condensation of low-V paqueite.* Paqueite forms by the reaction of melilite and minor aluminous phase(s) with vapor. The partial pressure of Ti in the vapor is greatly reduced.

(4) *Condensation of davisite–grossmanite.* These Sc-, Ti-enriched clinopyroxenes form by the reaction of paqueite  $\pm$  warkite and eringaite with vapor (source of V and Si). This process exhausts readily accessible eringaite. Some previously condensed perovskite and paqueite reequilibrate with vapor to become V-enriched or new V-rich grains of these phases.

(5) *Condensation of burnettite–kushiroite.* Where paqueite, warkite, and eringaite are unavailable, gehlenite reacts with vapor to form low-Ti, -Sc clinopyroxene (burnettite, kushiroite). Since these pyroxenes generally have Al/Ca ratios that are slightly higher than in gehlenite, an aluminous phase is likely also involved. Relative timing of events (4) and (5) is uncertain because the dominant difference is the presence or absence of previously condensed phases, which could be either spatially or temporally driven. The argument for paqueite undergoing this process follows from mass balance calculations suggesting that surviving V-free paqueites better fit the compositions of davisite–grossmanite than do V-enriched paqueites. Generally speaking, low-V phases

would be expected before (e.g., temperature is too high) and after (e.g., V is fully condensed) a limited time–space regime within which V-rich phases can be produced.

(6) *Condensation of diopside.* Although not discussed above, magnesian clinopyroxene is common in the outer regions of ultrarefractory inclusions (e.g., Ma et al., 2020) and it likely marks the beginning of condensation of Mg-rich phases.

Note that the above sequence does not include any thermal events leading to partial or complete melting. Such events would have post-dated the condensation processes outlined above (or they were spatially separated) and could have resulted in partial or complete destruction of the original condensate phases, depending mostly on when such phases were introduced into the proto-inclusion and the intensity of such thermal events. Moreover, grains may have been introduced or crystallized during one event and modified or destroyed in the next.

## SUMMARY AND CONCLUSIONS

Inclusions in melilite from type A inclusions did not all equilibrate with each other. Instead, they sampled a small number of discrete environments and reactions within a spectrum of processes and/or environments. Vanadium enrichment of phases included in melilite from type As generally predates formation and alteration of melilite in the current inclusion and can be used to infer relative timing in the production of observed inclusions, even if later melted and recrystallized. Paqueite initially condensed through the reaction of gehlenite with vapor and subsequently reacted with vapor and the ultrarefractory phases eringaite and warkite to produce davisite–grossmanite (and some Ti-, Sc-rich burnettite). In the absence of paqueite and the ultrarefractory phases, the reaction of melilite with vapor (source of V and Si) resulted in low Ti-, Sc- burnettite–kushiroite clinopyroxenes. The chemistry of *CGft-12* and A-WP1 inclusions in melilite generally reflects nebular processes. Timing for the introduction of what are now clinopyroxene and/or paqueite inclusions in melilite is unknown but likely late in a melting event when temperatures were sufficiently low that the condensate grains or melts whose compositions were dominated by former condensate grains could survive long enough to be incorporated into host melilite. Spinel in A-WP1 is exceptional in showing enrichment in V correlated with Fe that occurred during Fe-metasomatism. The alteration process appears to have mobilized V, so that secondary phases acquired some of the V originally present in some of the primary phases.

*Acknowledgments*—We gratefully acknowledge Philipp Heck for the loan of samples from the Field Museum of Chicago. SEM, EBSD, and EPMA analyses were carried out at the Caltech GPS Division Analytical Facility, which is supported, in part, by NSF Grants EAR-0318518 and DMR-0080065. We thank Marina Ivanova and associate editor Yves Marrocchi for their constructive reviews.

*Data Availability Statement*—Data available on request from the authors.

*Editorial Handling*—Dr. Yves Marrocchi

## REFERENCES

- Adams, L. H. 1914. Calibration Tables for Copper-Constantan and Platinum-Platinrhodium Thermocouples. *Journal of the American Chemical Society* 36: 65–72.
- Aléon, J., El Goresy, A., and Zinner, E. 2007. Oxygen Isotope Heterogeneities in the Earliest Presolar Gas Recorded in a Meteoritic Calcium-Aluminum-Rich Inclusion. *Earth and Planetary Science Letters* 263: 114–27.
- Aléon, J., Marin-Carbonne, J., McKeegan, K. D., and El Goresy, A. 2018. O, Mg, and Si Isotope Distributions in the Complex Ultrarefractory CAI Efremovka 101.1: Assimilation of Ultrarefractory, FUN, and Regular CAI Precursors. *Geochimica et Cosmochimica Acta* 232: 48–81.
- Allen, J. M., Grossman, L., Davis, A. M., and Hutcheon, I. D. 1978. Mineralogy, Textures and Mode of Formation of a Hibonite-Bearing Allende Inclusion. Proceedings, 9th Lunar and Planetary Science Conference. pp. 1209–33.
- Armstrong, J. T. 1995. CITZAF—A Package of Correction Programs for the Quantitative Electron Microbeam X-Ray-Analysis of Thick Polished Materials, Thin Films, and Particles. *Microbeam Analysis* 4: 177–200.
- Armstrong, J. T., El Goresy, A., and Wasserburg, G. J. 1985. Willy: A Prize Noble Ur-Fremdling—Its History and Implications for the Formation of Fremdlinge and CAI. *Geochimica et Cosmochimica Acta* 49: 1001–21.
- Barber, D. J., and Agrell, S. O. 1994. A New Titanium-Bearing Calcium Aluminosilicate Phase: III. Crystals from a Mixer Furnace Slag. *Meteoritics* 29: 691–5.
- Barber, D. J., Beckett, J. R., Paque, J. M., and Stolper, E. 1994. A New Titanium-Bearing Calcium Aluminosilicate Phase: II. Crystallography and Crystal Chemistry of Grains Formed in Slowly Cooled Melts with Bulk Compositions of Calcium-Aluminum-Rich Inclusions. *Meteoritics* 29: 682–90.
- Beckett, J. R., and Grossman, L. 1988. The Origin of Type C Inclusions from Carbonaceous Chondrites. *Earth and Planetary Science Letters* 89: 1–14.
- Beckett, J. R., Spivack, A. J., Hutcheon, I. D., Wasserburg, G. J., and Stolper, E. M. 1990. Crystal Chemical Effects on the Partitioning of Trace Elements Between Mineral and Melt: An Experimental Study of Melilite with Applications to Refractory Inclusions from Carbonaceous Chondrites. *Geochimica et Cosmochimica Acta* 54: 1755–74.
- Beckett, J. R., and Stolper, E. 1994. The Stability of Hibonite, Melilite and Other Aluminous Phases in Silicate Melts: Implications for the Origin of Hibonite-Bearing Inclusions from Carbonaceous Chondrites. *Meteoritics* 29: 41–65.
- Bischoff, A., Palme, H., Schultz, L., Weber, D., Weber, H. W., and Spettel, B. 1993. Acfer 182 and Paired Samples, an Iron-Rich Carbonaceous Chondrite: Similarities with ALH85085 and Relationship to CR Chondrites. *Geochimica et Cosmochimica Acta* 57: 2631–48.
- Burnett, D. S. 2006. NASA Returns Rocks from a Comet. *Science* 314: 1709–10.
- Burnett, D. S., Fowler, W. A., and Hoyle, F. 1965. Nucleosynthesis in the Early History of the Solar System. *Geochimica et Cosmochimica Acta* 29: 1209–41.
- Burnett, D. S., Jurewicz, A. J. G., Woolum, D. S., Wang, J., Paque, J. M., Nittler, L. R., McKeegan, K. D. et al. 2015. Ion Implants as Matrix-Appropriate Calibrators for Geochemical Ion Probe Analyses. *Geostandards and Geoanalytical Research* 39: 265–76.
- Burnett, D. S., and Wasserburg, G. J. 1967. <sup>87</sup>Rb-<sup>87</sup>Sr Ages of Silicate Inclusions in Iron Meteorites. *Earth and Planetary Science Letters* 2: 397–408.
- Burnett, D. S., and Woolum, D. S. 1977. Exposure Ages and Erosion Rates for Lunar Rocks. *Physics and Chemistry of the Earth* 10: 63–101.
- Caillet Komorowski, C. L. V., Zinner, E. K., McKeegan, K. D., Hervig, R., and Buseck, P. R. 2007. The White Angel: A Unique Wollastonite-Bearing, Mass-Fractionated Refractory Inclusion from the Leoville CV3 Carbonaceous Chondrite. *Meteoritics & Planetary Science* 42: 1159–82.
- Cameron, M., and Papike, J. J. 1981. Structural and Chemical Variations in Pyroxenes. *American Mineralogist* 66: 1–50.
- Campbell, A. J., Humayun, M., Meibom, A., Krot, A. N., and Keil, K. 2001. Origin of Zoned Metal Grains in the QUE 94411 Chondrite. *Geochimica et Cosmochimica Acta* 65: 163–80.
- Clarke, R. S., Jarosewich, E., Mason, B., Nelen, J., Gómez, M., and Hyde, J. R. 1971. The Allende, Mexico, Meteorite Shower. *Smithsonian Contributions to the Earth Sciences* 5: 1–53.
- Clayton, R. N., Hinton, R. W., and Davis, A. M. 1988. Isotopic Variations in the Rock-Forming Elements in Meteorites. *Philosophical Transactions of the Royal Society of London A* 325: 483–501.
- Connolly, H. C., and Burnett, D. S. 1999. A Study of the Minor Element Concentrations of Spinel from Two Type B Calcium-Aluminum-Rich Inclusions: An Investigation into Potential Formation Conditions of Calcium-Aluminum-Rich Inclusions. *Meteoritics & Planetary Science* 34: 829–48.
- Connolly, H. C., Burnett, D. S., and McKeegan, K. D. 2003. The Petrogenesis of Type B1 Ca-Al-Rich Inclusions: The Spinel Perspective. *Meteoritics & Planetary Science* 38: 197–224.
- Connolly, H. C., and Hewins, R. H. 1995. Chondrules as Products of Dust Collisions with Totally Molten Droplets Within a Dust-Rich Nebular Environment: An Experimental Investigation. *Geochimica et Cosmochimica Acta* 59: 3231–46.
- Davis, A. M., Kita, N. T., Ushikubo, T., MacPherson, G. J., Bullock, E. S., and Knight, K. B. 2010. Magnesium Isotopic Evolution of CAIs (Abstract #2496). 41st Lunar and Planetary Science Conference. CD-ROM.
- Deer, W. A., Howie, R. A., and Zussman, J. 1992. *An Introduction to Rock-Forming Minerals*, 2nd ed. Essex: Longman Scientific & Technical, 696 pp.

- Donovan, J. J., and Tingle, T. N. 1996. An Improved Mean Atomic Number Background Correction for Quantitative Microanalysis. *Microscopy and Microanalysis* 2: 1–7.
- Dowty, E., and Clark, J. R. 1973. Crystal Structure Refinement and Optical Properties of a  $Ti^{3+}$  Fassaite from the Allende Meteorite. *American Mineralogist* 58: 230–42.
- El Goresy, A., Palme, H., Yabuki, H., Nagel, K., Herrwerth, L., and Ramdohr, P. 1984. A Calcium-Aluminium-Rich Inclusion from the Essebi (CM2) Chondrite: Evidence for Captured Spinel-Hibonite Spherules and for an Ultra-Refractory Rimming Sequence. *Geochimica et Cosmochimica Acta* 48: 2283–98.
- El Goresy, A., Zinner, E., Matsunami, S., Palme, H., Spettel, B., Lin, Y., and Nazarov, M. 2002. Efremovka 101.1: A CAI with Ultrarefractory REE Patterns and Enormous Enrichments of Sc, Zr, and Y in Fassaite and Perovskite. *Geochimica et Cosmochimica Acta* 66: 1459–91.
- Fahey, A. J., Zinner, E. K., Crozaz, G., and Kornacki, A. S. 1987. Microdistributions of Mg Isotopes and REE Abundances in a Type A Calcium-Aluminum-Rich Inclusion from Efremovka. *Geochimica et Cosmochimica Acta* 51: 3215–29.
- Fairchild, D. P., Howden, D. G., and Clark, W. A. T. 2000. The Mechanism of Brittle Fracture in a Microalloyed Steel: Part I. Inclusion-Induced Cleavage. *Metallurgical and Materials Transactions A* 31A: 641–52.
- Floss, C., Nazarov, M. A. & Taylor, L. A. 2004. Rhönite-Bearing Inclusions E201 and E202 from Efremovka: Constraints from Trace Element Measurements (Abstract #9010). Workshop on Chondrites and Protoplanetary Disk.
- Fuchs, L. H. 1971. Occurrence of Wollastonite, Rhönite, and Andradite in the Allende Meteorite. *American Mineralogist* 56: 2053–68.
- Gasparik, T., Parise, J. B., Eiben, B. A., and Hriljac, J. A. 1995. Stability and Structure of a New High-Pressure Silicate  $Na_{1.8}Ca_{1.1}Si_6O_{14}$ . *American Mineralogist* 80: 1269–76.
- Grossman, L. 1975. Petrography and Mineral Chemistry of Ca-Rich Inclusions in the Allende Meteorite. *Geochimica et Cosmochimica Acta* 39: 433–54.
- Grossman, L., Ebel, D. S., Simon, S. B., Davis, A. M., Richter, F. M., and Parsad, N. M. 2000. Major Element Chemical and Isotopic Compositions of Refractory Inclusions in C3 Chondrites: The Separate Roles of Condensation and Evaporation. *Geochimica et Cosmochimica Acta* 64: 2879–94.
- Grossman, L., Simon, S. B., Rai, V. K., Thiemens, M. H., Hutcheon, I. D., Williams, R. D., Galy, A. et al. 2008. Primordial Compositions of Refractory Inclusions. *Geochimica et Cosmochimica Acta* 72: 3001–21.
- Hudon, P., Jung, I.-H., and Baker, D. R. 2005. Experimental Investigation and Optimization of Thermodynamic Properties and Phase Diagrams in the Systems  $CaO-SiO_2$ ,  $MgO-SiO_2$ ,  $CaMgSi_2O_6-SiO_2$  and  $CaMgSi_2O_6-Mg_2SiO_4$  to 1.0 GPa. *Journal of Petrology* 46: 1859–80.
- Jacobsen, B., Yin, Q.-Z., Moynier, F., Amelin, Y., Krot, A. N., Nagashima, K., Hutcheon, I. D., and Palme, H. 2008.  $^{26}Al$ - $^{26}Mg$  and  $^{207}Pb$ - $^{206}Pb$  Systematics of Allende CAIs: Canonical Solar Initial  $^{26}Al/^{27}Al$  Ratio Reinstated. *Earth and Planetary Science Letters* 272: 353–64.
- Jones, J. H., and Burnett, D. S. 1987. Experimental Geochemistry of Pu and Sm and the Thermodynamics of Trace Element Partitioning. *Geochimica et Cosmochimica Acta* 51: 769–82.
- Kaminskii, A. A., Belokoneva, E. L., Mill, B. V., Pisarevskii, Y. V., Sarkisov, S. E., Silvestrova, I. M., Butashin, A. V., and Khodzhabagyan, G. G. 1984. Pure and  $Nd^{3+}$ -Doped  $Ca_3Ga_2Ge_4O_{14}$  and  $Sr_3Ga_2Ge_4O_{14}$  Single Crystals, Their Structure, Optical, Spectral Luminescence, Electromechanical Properties, and Simulated Emission. *Physica Status Solidi, Section A: Applied Research* 86: 345–62.
- Katayama, J., Itoh, S., and Yurimoto, H. 2012. Oxygen Isotopic Zoning of Reversely Zoned Melilite Crystals in a Fluffy Type A Ca-Al-Rich Inclusions from the Vigarano Meteorite. *Meteoritics & Planetary Science* 47: 2094–106.
- Kawasaki, N., Itoh, S., Sakamoto, N., and Yurimoto, H. 2017. Chronological Study of Oxygen Isotope Composition for the Solar Protoplanetary Disk Recorded in Fluffy Type A CAI from Vigarano. *Geochimica et Cosmochimica Acta* 201: 83–102.
- Kawasaki, N., Sakamoto, N., and Yurimoto, H. 2012. Oxygen Isotopic and Chemical Zoning of Melilite Crystals in a Type A Ca-Al-Rich Inclusion of Efremovka CV3 Chondrite. *Meteoritics & Planetary Science* 47: 2084–93.
- Krot, A. N., Chaussidon, M., Yurimoto, H., Sakamoto, N., Nagashima, K., Hutcheon, I. D., and MacPherson, G. J. 2008. Oxygen Isotopic Compositions of Allende Type C CAIs: Evidence for Isotopic Exchange During Nebular Melting and Asteroidal Metamorphism. *Geochimica et Cosmochimica Acta* 72: 2534–55.
- Krot, A. N., Nagashima, K., Fintor, K., and Pál-Molnár, E. 2019. Evidence for Oxygen-Isotope Exchange in Refractory Inclusions from Kaba (CV3.1) Carbonaceous Chondrite During Fluid-Rock Interaction on the CV Parent Asteroid. *Geochimica et Cosmochimica Acta* 246: 419–35.
- Krot, A. N., Petaev, M. I., and Nagashima, K. 2021. Infiltration Metasomatism of the Allende Coarse-Grained Calcium-Aluminum-Rich Inclusions. *Progress in Earth and Planetary Science* 8: 61. <https://doi.org/10.1186/s40645-021-00437-4>.
- Krot, A. N., Yurimoto, H., Hutcheon, I. D., Chaussidon, M., MacPherson, G. J., and Paque, J. 2007. Remelting of Refractory Inclusions in the Chondrule-Forming Region: Evidence from Chondrule-Bearing Type C Calcium-Aluminum-Rich Inclusions from Allende. *Meteoritics & Planetary Science* 42: 1197–219.
- Kurat, G., Hoinkes, G., and Fredriksson, K. 1975. Zoned Ca-Al-Rich Chondrule in Bali: New Evidence Against the Primordial Condensation Model. *Earth and Planetary Science Letters* 26: 140–4.
- LaTourrette, T. Z., and Burnett, D. S. 1992. Experimental Determination of U and Th Partitioning Between Clinopyroxene and Natural and Synthetic Basaltic Liquid. *Earth and Planetary Science Letters* 110: 227–44.
- Lin, Y., and Kimura, M. 2003. Ca-Al-Rich Inclusions from the Ningqiang Meteorite: Continuous Assemblages of Nebular Condensates and Genetic Link to Type B Inclusions. *Geochimica et Cosmochimica Acta* 67: 2251–67.
- Lin, Y., Kimura, M., and Wang, D. 2003. Fassaite in Compact Type A Ca-Al-Rich Inclusions in the Ningqiang Carbonaceous Chondrite: Evidence for Partial Melting in the Nebula. *Meteoritics & Planetary Science* 38: 407–17.
- Lodders, K. 2002. Titanium and Vanadium Chemistry in Low-Mass Dwarf Stars. *Astrophysical Journal* 577: 974–85.



- Lodders, K. 2003. Solar System Abundances and Condensation Temperatures of the Elements. *Astrophysical Journal* 591: 1220–47.
- Ma, C. 2010. Hibonite-(Fe),  $(\text{Fe,Mg})\text{Al}_{12}\text{O}_{19}$ , a New Alteration Mineral from the Allende Meteorite. *American Mineralogist* 95: 188–91.
- Ma, C. 2013a. Paqueite, IMA 2013-053. CNMNC Newsletter No. 17, October 2013, Page 3002. *Mineralogical Magazine* 77: 2997–3005.
- Ma, C. 2013b. Burnettite, IMA 2013-054. CNMNC Newsletter No. 17, October 2013, Page 3002–3003. *Mineralogical Magazine* 77: 2997–3005.
- Ma, C. 2015. Nanomineralogy of Meteorites by Advanced Electron Microscopy: Discovering New Minerals and New Materials from the Early Solar System. *Microscopy and Microanalysis* 21: 2353–4.
- Ma, C. 2018. Discovery of Meteoritic Baghdadite,  $\text{Ca}_3(\text{Zr,Ti})\text{Si}_2\text{O}_9$ , in Allende: The First Solar Silicate with Structurally Essential Zirconium? (Abstract #6358). *Meteoritics & Planetary Science* 53.
- Ma, C., and Beckett, J. R. 2016. Burnettite,  $\text{CaVAISiO}_6$ , and Paqueite,  $\text{Ca}_3\text{TiSi}_2(\text{Al}_2\text{Ti})\text{O}_{14}$ , Two New Minerals from Allende: Clues to the Evolution of a V-Rich Ca-Al-Rich Inclusion (Abstract #1595). 47th Lunar and Planetary Science Conference. CD-ROM.
- Ma, C., Beckett, J. R., and Rossman, G. R. 2014a. Monipite,  $\text{MoNiP}$ , a New Phosphide Mineral in a Ca-Al-Rich Inclusion from the Allende Meteorite. *American Mineralogist* 99: 198–205.
- Ma, C., Beckett, J. R., and Rossman, G. R. 2014b. Allendeite ( $\text{Sc}_4\text{Zr}_3\text{O}_{12}$ ) and Hexamolybdenum (Mo, Ru, Fe), Two New Minerals from an Ultrarefractory Inclusion from the Allende Meteorite. *American Mineralogist* 99: 654–66.
- Ma, C., Krot, A. N., Beckett, J. R., Nagashima, K., Tschauer, O., Rossman, G. R., Simon, S. B., and Bischoff, A. 2020. Warkite,  $\text{Ca}_2\text{Sc}_6\text{Al}_6\text{O}_{20}$ , a New Mineral in Carbonaceous Chondrites and a Key-Stone Phase in Ultrarefractory Inclusions from the Solar Nebula. *Geochimica et Cosmochimica Acta* 277: 52–86.
- Ma, C., Krot, A. N., and Nagashima, K. 2017. Addibischhoffite,  $\text{Ca}_2\text{Al}_6\text{Al}_6\text{O}_{20}$ , a New Calcium Aluminate Mineral from the Acfer 214 CH Carbonaceous Chondrite: A New Refractory Phase from the Solar Nebula. *American Mineralogist* 102: 1556–60.
- Ma, C., Krot, A. N., Paque, J., Tschauer, O., and Nagashima, K. 2021. Beckettite,  $\text{Ca}_2\text{V}_6\text{Al}_6\text{O}_{20}$ , a New Mineral in a Type A Refractory Inclusion from Allende and Clues to Processes in the Early Solar System. *Meteoritics & Planetary Science* 56: 2265–72.
- Ma, C., and Rossman, G. R. 2008. Barioperovskite,  $\text{BaTiO}_3$ , a New Mineral from the Benitoite Mine, California. *American Mineralogist* 93: 154–7.
- Ma, C., and Rossman, G. R. 2009a. Tistarite,  $\text{Ti}_2\text{O}_3$ , a New Refractory Mineral from the Allende Meteorite. *American Mineralogist* 94: 841–4.
- Ma, C., and Rossman, G. R. 2009b. Davisite,  $\text{CaScAlSiO}_6$ , a New Pyroxene from the Allende Meteorite. *American Mineralogist* 94: 845–8.
- Ma, C., and Rossman, G. R. 2009c. Grossmanite,  $\text{CaTi}^{3+}\text{AlSiO}_6$ , A New Pyroxene from the Allende Meteorite. *American Mineralogist* 94: 1491–4.
- MacPherson, G. J., and Grossman, L. 1984. “Fluffy” Type A Ca-, Al-Rich Inclusions in the Allende Meteorite. *Geochimica et Cosmochimica Acta* 48: 29–46.
- Mendybaev, R. A., Kamibayashi, M., Teng, F.-Z., Savage, P. S., Georg, R. B., Richter, F. M., and Tachibana, S. 2021. Experiments Quantifying Elemental and Isotopic Fractionations During Evaporation of CAI-Like Melts in Low-Pressure Hydrogen and in Vacuum: Constraints on Thermal Processing of CAIs in the Protoplanetary Disk. *Geochimica et Cosmochimica Acta* 292: 557–76.
- Mendybaev, R. A., Richter, F. M., and Davis, A. M. 2006. Reevaluation of the Åkermanite-Gehlenite Binary System (Abstract #2268). 37th Lunar and Planetary Science Conference. CD-ROM.
- Mendybaev, R. A., Williams, C. D., Spicuzza, M. J., Richter, F. M., Valley, J. W., Fedkin, A. V., and Wadhwa, M. 2017. Thermal and Chemical Evolution in the Early Solar System as Recorded by FUN CAIs: Part II—Laboratory Evaporation of Potential CMS-1 Precursor Material. *Geochimica et Cosmochimica Acta* 201: 49–64.
- Mill, B. V., Butashin, A. V., and Éllern, A. M. 1983. Germanates with the  $\text{Ca}_3\text{Ga}_2\text{Ge}_4\text{O}_{14}$  Structure. *Inorganic Materials* 19: 1516–8.
- Paque, J. M. 1985. A Vanadium-Rich Fluffy Type A Ca-Al-Rich Inclusion in Allende (Abstract). 16th Lunar and Planetary Science Conference. pp. 651–2.
- Paque, J. M. 1987.  $\text{CaAl}_4\text{O}_7$  from Allende Type A Inclusion NMNH 4691 (Abstract). 43rd Lunar and Planetary Science Conference. pp. 762–3.
- Paque, J. M. 1989. Vanadium-Rich Refractory Platinum Metal Nuggets from a Fluffy Type A Inclusion in Allende (Abstract). 20th Lunar and Planetary Science Conference. pp. 822–3.
- Paque, J. M., Beckett, J. R., Barber, D. J., and Stolper, E. M. 1994. A New Titanium-Bearing Calcium Aluminosilicate Phase: I. Meteoritic Occurrences and Formation in Synthetic Systems. *Meteoritics* 29: 673–82.
- Paque, J. M., Beckett, J. R., and Burnett, D. S. 2008. Refractory Metal Nuggets as an Indicator of Alteration Processes in a V-rich Ca-Al-Rich Inclusion (Abstract #1841). 39th Lunar and Planetary Science Conference. CD-ROM.
- Paque, J. M., Beckett, J. R., Ishii, H. A., Aléon-Toppani, A., Burnett, D. S., Teslich, N., Dai, Z. R., and Bradley, J. P. 2009. The Formation of Boundary Clinopyroxenes and Associated Glass Veins in Type B1 CAIs. *Meteoritics & Planetary Science* 44: 665–87.
- Paque, J. M., Beckett, J. R., and Stolper, E. 1986. A New Ca-Al-Ti Silicate in Coarse-Grained Ca-Al-Rich Inclusions. 17th Lunar and Planetary Science Conference. pp. 646–7.
- Paque, J. M., Burnett, D. S., and Beckett, J. R. 2007. Zoning Patterns of Fe and V in Spinel from a Type B Ca-Al-Rich Inclusion: Constraints on Subsolvus Thermal History. *Meteoritics & Planetary Science* 42: 899–912.
- Paque, J. M., Lofgren, G. E., and Le, L. 2000. Crystallization of Calcium-Aluminum-Rich Inclusions: Experimental Studies on the Effects of Repeated Heating Events. *Meteoritics & Planetary Science* 35: 363–71.
- Paque, J. M., and Stolper, E. 1984. Crystallization Experiments on a Range of Ca-Al-Rich Inclusion Compositions. 15th Lunar and Planetary Science Conference. pp. 631–2.
- Paque, J. M., Sutton, S. R., Simon, S. B., Beckett, J. R., Burnett, D. S., Grossman, L., Yurimoto, H., Itoh, S., and Connolly, H. C. 2013. XANES and Mg Isotopic Analyses of Spinel in Ca-Al-Rich Inclusions: Evidence for Formation Under Oxidizing Conditions. *Meteoritics & Planetary Science* 48: 2015–43.

- Pouchou, J.-L., and Pichoir, F. 1991. Quantitative Analysis of Homogeneous or Stratified Microvolumes Applying the Model "PAP". In *Electron Probe Quantitation*, edited by K. F. J. Heinrich and D. E. Newbury, 31–75. New York: Plenum Press.
- Reinhardt, A., Zych, A., Köhler, I., and Albert, B. 2018. Disordered Langasites  $\text{La}_3\text{Ga}_5\text{MO}_{14}$ :  $\text{Eu}^{3+}$  ( $M = \text{Si, Ge, Ti}$ ) as Red-Emitting LED Phosphors. *Dalton Transactions* 47: 5703–13.
- Scheuermann, P., Kutoglu, A., Schosnig, M., and Hoffer, E. 2000. Structure and Stability of the High-Pressure Phase,  $\text{Ca}_3\text{TiSi}_2(\text{Al,Ti,Si})_3\text{O}_{14}$ . *American Mineralogist* 85: 784–91.
- Sharp, C. M., and Huebner, W. F. 1990. Molecular Equilibrium with Condensation. *Astrophysical Journal Supplement Series* 72: 417–31.
- Simon, S. B., Davis, A. M., and Grossman, L. 1996. A Unique Ultrarefractory Inclusion from the Murchison Meteorite. *Meteoritics & Planetary Science* 31: 106–15.
- Simon, S. B., Davis, A. M., and Grossman, L. 1999. Origin of Compact Type A Refractory Inclusions from CV3 Carbonaceous Chondrites. *Geochimica et Cosmochimica Acta* 63: 1233–48.
- Simon, S. B., Davis, A. M., and Grossman, L. 2001. Formation of Orange Hibonite, as Inferred from Some Allende Inclusions. *Meteoritics & Planetary Science* 36: 331–50.
- Simon, S. B., Grossman, L., and Davis, A. M. 1991. Fassaite Composition Trends During Crystallization of Allende Type B Refractory Inclusion Melts. *Geochimica et Cosmochimica Acta* 55: 2635–55.
- Simon, S. B., Sutton, S. R., and Grossman, L. 2007. Valence of Titanium and Vanadium in Pyroxene in Refractory Inclusion Interiors and Rims. *Geochimica et Cosmochimica Acta* 71: 3098–118.
- Srinivasan, G., Huss, G. R., and Wasserburg, G. J. 2000. A Petrographic, Chemical, and Isotopic Study of Calcium-Aluminum-Rich Inclusions and Aluminum-Rich Chondrules from the Axtell (CV3) Chondrite. *Geochimica et Cosmochimica Acta* 35: 1333–54.
- Stolper, E. 1982. Crystallization Sequences of Ca-Al-Rich Inclusions from Allende: An Experimental Study. *Geochimica et Cosmochimica Acta* 46: 2159–80.
- Stolper, E., and Paque, J. M. 1986. Crystallization Sequences of Ca-Al-Rich Inclusions from Allende: The Effects of Cooling Rate and Maximum Temperature. *Geochimica et Cosmochimica Acta* 50: 1785–806.
- Suzumura, A., Kawasaki, N., Seto, Y., Yurimoto, H., and Itoh, S. 2021. Origin of Minerals in Åkermanite-Rich Patch Texture and Oxygen Isotopic Evolution of Compact Type A Ca-Al-Rich Inclusions from the Northwest Africa 7865 CV Chondrite. *Geochimica et Cosmochimica Acta* 303: 51–65.
- Taran, M. N., and Ohashi, H. 2012. Optical Absorption Spectroscopy Study of Three Synthetic  $\text{V}^{3+}$ -Bearing Clinopyroxenes. *European Journal of Mineralogy* 24: 823–9.
- Teshima, J., and Wasserburg, G. J. 1985. Textures, Metamorphism and Origin of Type A CAI's (Abstract). 16th Lunar and Planetary Science Conference. pp. 855–6.
- Weber, D., and Bischoff, A. 1997. Refractory Inclusions in the CR Chondrite Acfer 059-EI Djouf 001: Petrology, Chemical Composition, and Relationship to Inclusion Populations in Other Types of Carbonaceous Chondrites. *Chemie der Erde* 57: 1–24.
- Wong, J., Lytle, F. W., Messmer, R. P., and Maylotte, D. H. 1984. K-Edge Absorption Spectra of Selected Vanadium Compounds. *Physical Review B* 30: 5596–610.

## SUPPORTING INFORMATION

Additional supporting information may be found in the online version of this article.

**Table S1** Calculated X-ray powder diffraction data for paqueite from the Allende CAI *A-WPI* ( $I_{\text{rel}} > 1$ ). The strongest reflections are given in bold.

**Table S2** Calculated X-ray powder diffraction data for burnettite from the Allende CAI *A-WPI* ( $I_{\text{rel}} > 1$ ). The strongest reflections are given in bold.